



AMERICAN METEOROLOGICAL SOCIETY

Journal of Physical Oceanography

EARLY ONLINE RELEASE

This is a preliminary PDF of the author-produced manuscript that has been peer-reviewed and accepted for publication. Since it is being posted so soon after acceptance, it has not yet been copyedited, formatted, or processed by AMS Publications. This preliminary version of the manuscript may be downloaded, distributed, and cited, but please be aware that there will be visual differences and possibly some content differences between this version and the final published version.

The DOI for this manuscript is doi: 10.1175/2008JPO3740.1

The final published version of this manuscript will replace the preliminary version at the above DOI once it is available.



An Adjoint Sensitivity Analysis of the Southern California Current Circulation and Ecosystem. Part I: The Physical Circulation

Andrew M. Moore¹, Hernan G. Arango², Emanuele Di Lorenzo³,
Arthur J. Miller⁴,
and Bruce D. Cornuelle⁴

¹ Department of Ocean Sciences, 1156 High Street
University of California, Santa Cruz CA 95062.

² Institute of Marine and Coastal Sciences, Rutgers University,
71 Dudley Road, New Brunswick NJ 08901-8521.

³ School of Earth and Atmospheric Sciences,
Georgia Institute of Technology, Atlanta GA 30332-0340.

⁴ Climate Research Division, Scripps Institute of Oceanography,
University of California, San Diego, La Jolla CA 92093-0224.

July 16, 2008



Abstract

Adjoint methods of sensitivity analysis were applied to the California Current using the Regional Ocean Modeling Systems (ROMS) with medium resolution, aimed at diagnosing the circulation sensitivity to variations in surface forcing. The sensitivities of coastal variations in SST, eddy kinetic energy, and baroclinic instability of complex time evolving flows were quantified. Each aspect of the circulation exhibits significant interannual and seasonal variations in sensitivity controlled by mesoscale circulation features. Central California SST is equally sensitive to wind stress and surface heat flux, and less so to wind stress curl, displaying greatest sensitivity when upwelling favorable winds are relaxing, and least sensitivity during the peak of upwelling. SST sensitivity is typically 2-4 times larger during Summer than during Spring, although larger variations occur during some years.

The sensitivity of central coast eddy kinetic energy to surface forcing is on average constant throughout the year. Perturbations in the wind that align with mesoscale eddies to enhance the strength of the circulation by local Ekman pumping yield the greatest sensitivities.

The sensitivity of the potential for baroclinic instability is greatest when nearshore horizontal temperature gradients are largest, and is associated with variations in wind stress concentrated along the core of the California Current. The sensitivity varies by a factor ~ 1.5 throughout the year. A new and important aspect of this work is identification of the complex flow dependence and seasonal dependence of the sensitivity of the ROMS CCS circulation to variations in surface forcing that was hitherto not previously appreciated.



1 Introduction

The California Current System (CCS) is a complex eastern boundary current (Hickey, 1979; 1998), and there remain many unanswered questions concerning the underlying dynamics of the circulation (Miller *et al.*, 1999). There have been a number of recent efforts to establish permanent operational real-time observing systems along the entire west coast of the U.S. (*i.e.* the Southern California Coastal Ocean Observing System (SCCOOS) and the Central California Coastal Ocean Observing System (CenCOOS)). In addition there exist a number of rich historical data sets for both the physical and biological environment (*i.e.* the California Cooperative Fisheries Investigation (CalCOFI)). Efforts are also underway to set up a real-time ocean forecasting system for parts of the CCS (Chao *et al.*, 2007; Li *et al.*, 2007) and real-time data, both in-situ and satellite data, are a critical for this effort. Important aims for the current observation and forecasting programs include: (i) providing a more complete picture of the CCS circulation; (ii) elucidating the dynamics of the CCS; (iii) understanding the impact of the physical environment on local ocean ecosystems; and (iv) providing routine ocean forecasts in support of various government agency and public service activities.

Ocean state estimates for studies of ocean dynamics and routine ocean forecasting are generated using data assimilation techniques. Any data assimilation efforts in the CCS must necessarily be built upon a sound knowledge of the physical attributes that control the circulation in the forecast region. If the model is reliable, these same attributes will control the circulation in the real ocean also. Therefore a detailed sensitivity analysis of the CCS circulation serves several purposes.

We begin with a brief description of the physical circulation of the southern CCS. A dom-



inant feature of the CCS is near-shore upwelling and its rich coastal ecosystems. The coastal upwelling is primarily driven by alongshore winds (Bakun, 1990), although the character of the winds varies with latitude. South of Point Reyes (see Fig. 1a) the alongshore winds are upwelling favourable all year round, while to the north, upwelling (downwelling) winds exist only during the Summer (Winter). Since the focus of the present study is the southern portion of the CCS we describe only the main features of the circulation in this region. Excellent reviews of the entire CCS circulation can be found in Hickey (1979; 1998).

South of Point Reyes, the CCS is comprised of the equatorward California Current (CC), a persistent undercurrent, and intermittent near shore countercurrents. The circulation is also dominated by mesoscale eddies and filaments which are apparent from drifters, and in the surface thermal structure and ocean surface color (e.g. Abbot and Zion, 1985; Strub *et al.*, 1991; Swenson *et al.*, 1992; Strub and James, 2000).

There have been numerous modeling and diagnostic studies of the CCS, and many indicate that local variations in the surface wind play an important role in controlling the circulation (e.g. Allen, 1980; McCreary *et al.*, 1987; Brink, 1991; Batteen, 1997; Oey, 1999; Di Lorenzo, 2003). Observations and models also indicate that the CCS is characterized by several dynamical regimes, including Rossby wave dynamics (e.g. Strub and James, 2000; Di Lorenzo, 2003), mesoscale eddy variability (e.g. Kelly *et al.*, 1998), and instabilities associated with near-shore density fronts (Strub and James, 2000). Several prominent topographic features (Point Arena, Cape Mendocino, Point Reyes, Point Conception, see Fig. 1a) also play a significant role in shaping local circulation patterns (Batteen, 1997), particularly in relation to the formation of filaments and eddies (e.g. Enriquez and Friehe, 1995; Marchesiello *et al.*, 2003).

The numerous complex and often competing dynamical regimes can render difficult the



interpretation of CCS observations and model simulations. In addition, there are other potentially important factors such as the influence of stochastic forcing on the CCS that have received little attention, although they are believed to be important in the ocean (e.g. Frankignoul and Müller, 1979; Müller and Frankignoul, 1981; Aiken *et al.*, 2002; Chhak *et al.*, 2006a,b; Chhak and Moore, 2007; Chhak *et al.*, 2008).

Despite the large body of observation and modeling literature on the CCS, there has been no systematic quantitative exploration of the sensitivities of fundamental aspects of the CCS circulation to the various inputs of the system. Therefore, in this paper we have used the adjoint of an ocean general circulation model in an attempt to unravel the competing influences of various physical aspects of the CCS circulation. While some fundamental aspects of the CCS circulation have been documented and are well understood, such as the role of the alongshore wind stress in promoting upwelling and in establishing cross-shelf pressure gradients that drive the primary current systems, quantitative questions remain about the sensitivity of the circulation to the timing and structure of variations in the forcing. The analyses presented here shed new and important light on these sensitivities which are relevant to our understanding of the CCS and efforts to predict the circulation. Furthermore, the temporal and spatial nature of these sensitivities as revealed by the adjoint method are unique and unknown *a priori*. The only other way that they can be obtained is via direct numerical simulations involving a very large number of costly forward model integrations.

We consider three dynamical aspects of the CC that have received considerable attention, namely: coastal upwelling and sea surface temperature (SST), eddy kinetic energy, and baroclinic instability. We demonstrate that while many of the qualitative conclusions reported elsewhere are validated by the adjoint approach, the current study is able to formally *quantify*



the sensitivities to surface forcing, and reveals additional, more subtle aspects of the circulation sensitivities. The biological aspects will be explored in Part II. Adjoint techniques have been used extensively for sensitivity analysis in meteorology (e.g. Hall and Cacuci, 1983; Langland *et al.*, 1995; Rabier *et al.*, 1996) and other branches of physics (Cacuci, 1981ab), but have only recently found favor in oceanography (e.g. Junge and Haine, 2001; Galanti and Tziperman, 2003).

A description of the ocean model follows in section 2. The model physical circulation is discussed in section 3, and in sections 4 and 5 we introduce the adjoint method of sensitivity analysis which is applied in sections 6 and 7 to various indices that characterize different physical aspects of the circulation. We end with a summary and conclusions in section 8.

2 The Regional Ocean Modeling System

The primary tools used in the present study are a coupled physical-biological ocean model comprised of the Regional Ocean Modeling System (ROMS) and a 4-component nitrogen-based trophic model. ROMS is a state-of-the-art hydrostatic, free-surface ocean general circulation model developed specifically for regional applications (Haidvogel *et al.*, 2000, 2008). The model uses a terrain following coordinate system in the vertical, and generalized orthogonal curvilinear coordinates in the horizontal with the result that the complex topography and bathymetry often encountered in coastal regions can be well resolved (Shchepetkin and McWilliams, 2004).

In addition ROMS is equipped with a comprehensive suite of open boundary conditions (Marchesiello *et al.*, 2001) and can be conveniently nested with varying resolution.

The model domain extends from 115°W to 132°W, 29°N-39.5°N (Fig. 1b). The horizontal



resolution is 20 km and there are 20 s-levels in the vertical. The effective vertical resolution varies spatially: $\sim 5 - 10$ m along the shelf, and offshore between ~ 10 m near the surface and ~ 1200 m in the deep ocean. At the open boundaries, a clamped boundary condition was used to constrain the tracer and velocity fields using the solution from a larger domain configuration ($152 - 110^\circ\text{W}$, $24.5 - 48^\circ\text{N}$) with the same resolution.¹ Radiation conditions were imposed on the free-surface and barotropic velocity following Chapman (1985) and Flather (1976). Since the Flather and Chapman radiation conditions do not conserve mass, a volume conservation constraint was imposed following Marchesiello *et al.* (2001) to compensate for any average loss or gain of mass through the open boundaries. No-slip conditions were imposed at all coastal boundaries on velocity, and zero gradient conditions on all tracers.

Both model domains employ the same physical parameterizations and numerical algorithms including: a non-linear equation of state; 3rd-order upstream horizontal advection of momentum, temperature, salinity and biological tracers; KPP vertical mixing (Large *et al.*, 1994); and horizontal mixing of temperature, salinity and momentum along s-surfaces. The biological model employed was a standard 4-component nitrogen-based (NPZD) trophic model (Franks, 2002; Powell *et al.*, 2006) and is described in detail in Part II.

The horizontal resolution employed here is less than typically used to model this region, for two reasons. The first is a practical consideration and stems from the fact that at the time these calculations were performed, a parallel version of the ROMS adjoint was not available.

¹Additional experiments were performed using a sponge layer in conjunction with clamped boundaries to alleviate potential problems associated with over-specification of boundary conditions (Marchesiello *et al.*, 2001). The findings and conclusions of sensitivity analyses reported in later sections are insensitive to the presence of the sponge layer, so only those experiments performed without a sponge layer are presented here.



Secondly, the primary focus of this study was to explore the sensitivity of the broad, persistent, mesoscale features of the CCS circulation to variations in surface forcing. Estimates of the 1st baroclinic mode radius of deformation for the region range from ~ 15 km (Barth, 1994) to ~ 20 – 40 km (Emery *et al.*, 1984; Chelton *et al.*, 1998), so the chosen 20 km gridspacing is close to the mid-range. Furthermore, recent CCS modeling studies using ROMS at resolutions ranging from 3.5 km to 20 km by Marchesiello *et al.* (2003) and 0.75 km to 12 km by Capet *et al.* (2008) indicate that the broadest mesoscale features and mean seasonal circulation are relatively insensitive to horizontal grid resolution, and that the transition to submesoscale resolution (Capet *et al.*, 2008) does not significantly alter the dominant mesoscale flow structures.

The adjoint methods employed here are predicated on the tangent linear (TL) assumption, and provide reliable sensitivity information for finite-amplitude perturbations only while the TL assumption is valid. Experience has shown that as model resolution increases the time interval over which the TL assumption is valid decreases as smaller scale, nonlinear circulation features emerge. Therefore we expect the adjoint method to become increasingly limited in time for finite-amplitude perturbations at ever increasing model resolutions. However, given these caveats, we feel comfortable using 20 km resolution to explore the sensitivity of the broad, persistent, energetic components of the CCS mesoscale since the model captures these important features of the circulation (as demonstrated in section 3), and the TL assumption for finite-amplitude perturbations is valid for dynamically relevant time intervals. However, all that said, some of the sensitivity results presented in the following sections and their interpretation are likely to be model resolution dependent.

Another focus of this study is the influence of natural, unforced, internal variations in the ocean mesoscale circulation on the circulation sensitivities. With this in view our aim was



to create a large-scale circulation environment on which the mesoscale circulation can develop naturally and evolve. For this reason, ROMS was forced with monthly mean surface wind stress and surface fluxes of heat and freshwater derived from the NCEP/NCAR reanalysis project (Kalnay *et al.*, 1996) which captures the influence of the large-scale atmospheric circulation environment on the ocean. In addition, NCEP forcing is devoid of localized forcing features that may force localized variability, features of the circulation that we wish to exclude for the moment. Despite this apparent shortcoming of the NCEP forcing products, Di Lorenzo *et al.* (2008) have demonstrated that when forced by NCEP forcing products, ROMS captures much of the observed upper ocean variability in temperature, salinity and nutrient along the eastern boundary of the North Pacific using similar resolution (15 km) to that used here. That said, similar results (not reported here) to those described in sections 6 and 7 were obtained using a higher resolution (~ 10 km) wind product derived from the Navy's Coupled Ocean/Atmosphere Mesoscale Prediction System (COAMPS).

3 The Physical Model Circulation

The model open boundaries were constrained by the circulation from the large domain spun-up for 50 years using the NCEP forcing starting from a state of rest and Levitus climatological temperature and salinity distributions, the large domain constrained at its boundaries by a combination of radiation conditions and relaxation to Levitus temperature and salinity climatology (Di Lorenzo *et al.*, 2004). The model used for the sensitivity calculations was initialized on 1 Jan, year 1 using the year 50 large domain solution, and run for 10 years.

Figure 2a shows the April mean SST during maximum coastal upwelling. During Fall



and Winter (Fig. 2b), SST increases as the rate of upwelling decreases. Figure 2 also shows snap-shots of SST and sea surface height (SSH) on 1 April and 1 Oct of year 6, and indicates that there is considerable mesoscale eddy variability qualitatively similar to that observed. SSH (Figs. 2d and 2f) is a good surrogate for surface geostrophic currents and the southward flowing CC is clearly apparent. Typical filament and eddy features are labelled “F”, “e₁” and “e₂” in Figs. 2e and 2f, and have scales ranging 100 km in the case of “F” to 200 – 350 km for “e₁” and “e₂.” These can be considered as the smallest resolvable mesoscale features to which the results of the sensitivity analyses presented in later sections apply.

Vertical sections of monthly mean April and Oct. temperature and alongshore velocity along the line indicated in Fig.2e are shown in Fig. 3. The seasonal signature of upwelling is evident with, for example, the 12°C isotherm outcropping near 123°W in April (Fig. 3a) and along the coast in Oct (Fig. 3b). Observations show that the CC is confined to the upper 500m (Hickey, 1998), with seasonal mean speeds $\sim 0.1 \text{ m s}^{-1}$ and maximum velocities in Summer to early Fall. The model CC (Figs. 3c and 3d) has a broad vertical extent with peak speeds at the surface of $\sim 0.2 \text{ m s}^{-1}$, decreasing rapidly over the upper 200 m, reaching peak surface speeds in the Spring and early Summer, depending on latitude. Observations suggest that the undercurrent is narrow ($\sim 10 - 40 \text{ km}$) flowing poleward over the continental slope, with peak speeds of $0.3 - 0.5 \text{ m s}^{-1}$ in Summer and early Fall in the depth range 100 – 300 m. The undercurrent is poorly resolved by the model used here, although there is a weak ($\sim 0.1 \text{ m s}^{-1}$), poleward flow over the shelf against the coast, present year round below the surface, in general agreement with observations (Hickey, 1998).



4 Adjoint Sensitivity Analysis

We denote the ROMS state vector as $\Phi(t) = (\mathbf{u} \ \mathbf{v} \ \mathbf{T} \ \mathbf{S} \ \zeta \ \mathbf{N} \ \mathbf{P} \ \mathbf{Z} \ \mathbf{D})^T$, where \mathbf{u} , \mathbf{v} , \mathbf{T} , \mathbf{S} , ζ , \mathbf{N} , \mathbf{P} , \mathbf{Z} , \mathbf{D} are vectors of the model grid point values at time t of zonal velocity, meridional velocity, temperature, salinity, SSH, nitrate, phytoplankton, zooplankton and detritus respectively, and superscript T denotes the transpose. Thus $\Phi(t)$ is a vector comprised of all model prognostic variables at a single time. The nonlinear ROMS (hereafter denoted NLROMS) will be represented symbolically by:

$$\partial\Phi/\partial t = \mathcal{M}(\Phi) + \mathbf{f}(t) \quad (1)$$

where \mathcal{M} denotes all model linear and nonlinear operators, and $\mathbf{f}(t)$ is the forcing. Equation (1) is solved subject to initial condition $\Phi(t_i) = \Phi_i$ and boundary conditions $\Phi_\Omega(t)$ where Ω denotes all boundaries, open and closed.

For sensitivity analysis a scalar function $J = G(\Phi(t))$ serves as an indicator of some aspect of the circulation, and the sensitivity of J to variations in $\Phi(t)$, Φ_i , $\Phi_\Omega(t)$ and $\mathbf{f}(t)$ is explored (Cacuci, 1980a,b). Let $\Phi_0(t)$ represent the solution of (1) that describes the time evolving CCS, and consider perturbations $\delta\Phi(t)$ to $\Phi_0(t)$ arising from small perturbations $\delta\Phi_i$, $\delta\Phi_\Omega(t)$ and $\delta\mathbf{f}(t)$ to the initial conditions, boundary conditions and forcing respectively. To first-order:

$$\partial\delta\Phi/\partial t = \left(\left. \partial\mathcal{M}(\Phi)/\partial\Phi \right|_{\Phi_0(t)} \right) \delta\Phi + \delta\mathbf{f}(t) \quad (2)$$

subject to $\delta\Phi_i$ and $\delta\Phi_\Omega(t)$. Equation (2) is referred to as the Tangent Linear ROMS (TL-ROMS), and compact solutions may be written as:

$$\delta\Phi(t_f) = \mathbf{R}(t_i, t_f)\delta\Phi(t_i) + \int_{t_i}^{t_f} \mathbf{R}(\tau, t_f)\mathbf{P}\delta\mathbf{f}(\tau)d\tau \quad (3)$$

where $\mathbf{R}(t_i, t_f)$ is the propagator for the interval $[t_i, t_f]$. $\mathbf{f}(t)$ is imposed as flux surface boundary conditions on tracers and momentum denoted here by the matrix operator \mathbf{P} in (3). Forcing perturbations $\delta\mathbf{f}$ are transformed by \mathbf{P} into perturbations $\delta\Phi = \mathbf{P}\delta\mathbf{f}$ that are advanced in time by \mathbf{R} according to the second term on the right hand side of (3).

Using (3), the resulting change $\delta J \simeq \delta\Phi^T(\partial J/\partial\Phi)$ in J is given by:

$$\delta J(t) = \delta\Phi^T(t_i)\mathbf{R}^T(t, t_i)\partial G/\partial\Phi(t) + \Delta t \sum_{j=0}^N \delta\mathbf{f}^T(t_i + j\Delta t)\mathbf{P}^T\mathbf{R}^T(t, t_i + j\Delta t)\partial G/\partial\Phi(t) \quad (4)$$

where for later convenience the integral in (3) is written as a Riemann sum, Δt is the ROMS timestep, and $t = t_i + N\Delta t$. In (4), $\mathbf{R}^T(t, t_i)$ represents the propagator of the adjoint of TLROMS (referred to hereafter as ADROMS), and the re-ordered time arguments denote integration backwards in time.

Solutions of TLROMS and ADROMS do not depend explicitly on the forcing $\mathbf{f}(t)$ of NLROMS (1); they depend only on $\Phi_0(t)$ as driven by $\mathbf{f}(t)$. This is because $\mathbf{f}(t)$ is independent of the model prognostic variables as formulated here². The perturbations $\delta\mathbf{f}(t)$ in TLROMS (2) can therefore be divorced from $\mathbf{f}(t)$ in as much as they can be viewed as arbitrary perturbations to the surface boundary conditions in the presence of the circulation $\Phi_0(t)$.

²In general of course $\mathbf{f}(t)$ will be an explicit function of the ocean circulation due to the influences of the latter on the atmospheric surface boundary layer. Such complications are not considered here.



In the limit $\delta\Phi(t_i) \rightarrow 0$ and $\delta\mathbf{f}(t) \rightarrow 0$, equation (4) indicates that:

$$\partial J(t)/\partial\Phi(t_i) = \mathbf{R}^T(t, t_i)\partial G/\partial\Phi(t); \quad \partial J(t)/\partial\mathbf{f}(t_i + j\Delta t) = \Delta t\mathbf{P}^T\mathbf{R}^T(t, t_i + j\Delta t)\partial G/\partial\Phi(t). \quad (5)$$

The gradient vectors $\partial J(t)/\partial\Phi(t_i)$ and $\partial J(t)/\partial\mathbf{f}(t_i + j\Delta t)$ reflect the sensitivity of J to changes in Φ_i and $\mathbf{f}(t_i + j\Delta t)$, and (5) shows they can be evaluated by integrating $\partial G/\partial\Phi(t)$ backwards in time using ADROMS.

The gradient vectors can be expressed as linear superpositions of the singular vectors (SVs) of the tangent linear propagator \mathbf{R} as shown by Gelaro *et al.* (1998). As such the structure of the gradient vectors will be largely dictated by the fastest growing SVs which are themselves closely tied to individual circulation features because they achieve rapid growth via barotropic and baroclinic instability and linear eigenmode interference (Farrell and Ioannou, 1996). The close connection between the gradient vectors and the leading SVs means that we can also interpret the former as perturbations that yield large changes in J , an idea that we exploit in sections 6 and 7.

As noted above, adjoint sensitivity analysis is predicated on the validity of the TL assumption. A suite of experiments using the SVs as perturbations for NLROMS and TLROMS (not shown) indicate that for finite-amplitude perturbations that achieve dynamically relevant amplitudes (*i.e.* $\zeta \sim 0.11$ m, $(u, v) \sim 0.4$ m s⁻¹, and SST $\sim 1.5^\circ\text{C}$), the TL assumption is valid for ~ 30 days.



5 Physical Processes of Interest

Despite the body of literature on the qualitative nature of the role surface forcing plays in controlling the CCS, there have been few quantitative studies. These have either been of somewhat limited scope and/or using idealized models (e.g. Allen, 1980; Brink, 1991; McCreary *et al.*, 1991; Auad *et al.*, 1991; Batteen, 1997), or have concentrated on circulation differences that result from different forcing products (e.g. Di Lorenzo, 2003; Marchesiello *et al.*, 2003). Here we are specifically interested in exploring, in a rigorous quantitative framework, the spatio-temporal variations in the sensitivity of some dominant physical aspects of the CCS circulation. With this in mind, we consider three scalar functions as heuristic indicators of upwelling, kinetic energy, and baroclinic instability.

5.1 J_{SST} : Coastal SST and Upwelling

As a measure of the strength of the upwelling, we computed an index J_{SST} based on the space-time averaged SST, namely:

$$J_{\text{SST}} = \frac{1}{A(t_f - t_i)} \int_A \int_{t_i}^{t_f} (\text{SST} - \gamma \overline{\text{SST}})^2 dt dA \quad (6)$$

where an overbar represents the NLROMS monthly mean, and A is the area enclosed by the target region shown in Fig. 2a where coastal upwelling in the model is most pronounced. The coefficient $\gamma = 0$ or 1 depending on whether the index is based on SST or SST anomaly, and $(t_f - t_i) = 30$ days in accordance with the TL assumption. Timeseries of J_{SST} are shown in Fig. 4a. For $\gamma = 0$ the seasonal cycle of upwelling dominates with minimum SST in Spring and maximum SST in Fall, while $\gamma = 1$ captures mesoscale variability and interannual variations.



Since J_{SST} involves a time average, the gradient vectors in (5) are modified as described in the Appendix. In addition, we are generally interested in the sensitivity of J_{SST} to variations in the time mean forcing $\bar{\mathbf{f}}$ and variations in wind stress curl, as described in the Appendix.

5.2 J_{KE} : Eddy Kinetic Energy

We define an index of kinetic energy so that:

$$J_{\text{KE}} = \frac{\rho_o}{2LA(t_f - t_i)} \int_L \int_A \int_{t_i}^{t_f} ((u - \gamma\bar{u})^2 + (v - \gamma\bar{v})^2) dt dA dz \quad (7)$$

where $\int_L dz$ denotes the depth integral $\sim 0 - 300$ m, and $t_f - t_i = 30$ days. The target area A used for J_{KE} (Fig. 2b) is independent of that used for J_{SST} and coincides with the area of maximum observed eddy kinetic energy (EKE) (see Marchesiello *et al.*, 2003, Fig. 13d, and Kelly *et al.*, 1998, Plate 1). Model EKE is maximum here also and more tightly confined to the coast than observed, but consistent in spatial extent and magnitude with surface values of Marchesiello *et al.* (2003) computed at the same resolution. Timeseries of J_{KE} for $\gamma = 0$ and 1 (Fig. 4b) exhibit considerable variability associated with mesoscale circulations with no pronounced seasonal cycle, although during some years there is a tendency for high (low) KE in Summer and Fall (Winter and Spring), consistent with observations (*e.g.* Kelly *et al.*, 1998; Strub and James, 2000).

5.3 $J_{\sigma_{\text{BI}}}$: Baroclinic Instability

It is widely believed that baroclinic instability promotes eddy variability in the CCS (see Strub and James (2000) and references therein). A measure of the potential for baroclinic instability



commonly used in meteorology and oceanography is the maximal Eady mode growth rate, the so-called “Eady Index,” denoted $\sigma_{BI} = 0.31f|\partial\mathbf{v}/\partial z|N^{-1}$ (e.g. Lindzen and Farrell, 1980; Hoskins and Valdes, 1990; Chelton *et al.*, 2006), where f is the Coriolis parameter, and N is the spatially varying Brunt-Väisälä frequency. We will consider:

$$J_{\sigma_{BI}} = \frac{1}{LA(t_f - t_i)} \int_L \int_A \int_{t_i}^{t_f} \sigma_{BI}^2 dt dA dz \quad (8)$$

as an index of the potential for baroclinic instability, where L , A and $(t_f - t_i)$ are identical to those used for J_{KE} . A timeseries of $J_{\sigma_{BI}}$ (Fig. 4c) indicates that the circulation in the target volume is most (least) susceptible to baroclinic instability during Spring (Fall). The average e-folding time of the fastest growing Eady mode (or equivalently the Charney mode (Gill, 1982)) in the target region is ~ 3 days consistent with theoretical studies (e.g. the “traditional baroclinic instability” modes identified by Barth (1994) with peak e-folding times of 3.3 days and wavelengths ~ 100 km), but somewhat shorter than the ~ 5 day e-folding time inferred from climatological observations (Chelton *et al.*, 2006). Observational estimates of σ_{BI} are typically based on averages of N and $|\partial\mathbf{v}/\partial z|$ over the upper ~ 1000 m, while in the model spatially varying N and \mathbf{v} are used. Nonetheless, trends in σ_{BI} are probably a useful indicator of time variations in the potential for baroclinic instability, despite the over simplification of the Eady and Charney models.

6 Coastal SST and Upwelling Sensitivity (J_{SST})

Adjoint sensitivity calculations aimed at exploring the monthly sensitivities of J_{SST} to variations in surface forcing were initiated on day 1 of each month during the last 5 years of the



NLROMS simulation of section 3. The time-dependent gradient vectors $\partial J/\partial \mathbf{f}$ represent the sensitivity of J_{SST} to independent perturbations in each gridpoint element of $\mathbf{f} = (f)$. However, the units of $\partial J/\partial \mathbf{f}$ vary across components complicating the direct comparison of the sensitivities. Therefore in order to compare directly the sensitivity of J_{SST} to perturbations in each element of \mathbf{f} , we considered the changes $\Delta J_i = \Delta f \partial J/\partial f_i$ that would result from perturbations Δf at each gridpoint i within the target region³ over the interval $[t_i, t_f]$. The standard deviations of each element of \mathbf{f} averaged over the target region were used as typical forcing perturbation amplitudes Δf . To summarize the sensitivities $\Delta J_{\text{SST}} = (1/n \sum_{i=1}^n \Delta J_i^2)^{1/2}$ was computed where n is the number of gridpoints enclosed by the target region.

A direct comparison of ΔJ_{SST} arising from perturbations in each component of surface forcing (τ , Q , $E - P$) therefore provides an immediate quantitative appreciation of the sensitivity of J_{SST} to perturbations with amplitudes typical of those encountered in the real ocean. To illustrate, Fig. 5 shows time series of ΔJ_{SST} for the last 5 years of the model integration for $(t_f - t_i) = 30$ days for $\gamma = 0$ and $\gamma = 1$. Figure 5 indicates that J_{SST} is approximately equally sensitive to variations in $\bar{\tau}$ and \bar{Q} , and less so to variations in curl $\bar{\tau}$, where an overbar denotes a monthly mean. For all J considered, the sensitivity to variations in the surface freshwater flux was negligible and will not be considered further.

An important test of the methodology is presented in Fig. 6 showing vectors of $(\partial J_{\text{SST}}/\partial \bar{\tau}_x, \partial J_{\text{SST}}/\partial \bar{\tau}_y)$ for Oct year 6 for $\gamma = 0$ and $\gamma = 1$, a time when Figs. 5b and 5e reveal that J_{SST} is generally most sensitive to variations in $\bar{\tau}$. As anticipated *a priori*, for $\gamma = 0$ (Fig. 6a) an increase (decrease) in upwelling favorable winds leads to a decrease (increase) in J_{SST} ,

³Analyses revealed that the largest values of $\partial J_{\text{SST}}/\partial f$ typically occur primarily within the target region.



indicating that ADROMS yields the correct sensitivity. However, what was not anticipated is the considerable spatio-temporal variation in the circulation sensitivities to variations in $\bar{\tau}$. For example, Fig. 6a shows that the maximum sensitivities extend $\sim 150 - 200$ km offshore, are not spatially uniform, and extend outside the target region. This is the case at other times of the year also (not shown), with sensitivity features tied to the mesoscale circulation structure. For $\gamma = 1$ (Fig. 6b) J_{SST} is defined in terms of SST anomalies, and the sensitivity vectors are more locally confined.

Temporal variations in $(\partial J/\partial\bar{\tau}_x, \partial J/\partial\bar{\tau}_y)$ reveal that the region of maximum sensitivity sometimes propagates offshore indicating a sensitivity to wind stress curl. Figures 7a and 7c show a close-up view of the sensitivity vectors associated with the periods 0-5 Oct and 21-25 Oct, year 6. Notice how J_{SST} is more sensitive to alongshore variations in $\bar{\tau}$ offshore during the penultimate week of Oct (Fig. 7c), and more sensitive to alongshore winds close to the shore during the first week (Fig. 7a). These changes are accompanied by a change in $\partial J_{\text{SST}}/\partial\text{curl}\bar{\tau}$ as shown in Figs. 7b and 7d. As anticipated *a priori*, over much of the target region a decrease (increase) in wind stress curl is associated with an increase (decrease) in SST due to the associated decrease (increase) in upwelling, indicating that ADROMS yields the correct result. However, the spatio-temporal variations in $\partial J_{\text{SST}}/\partial\text{curl}\bar{\tau}$ in Fig. 7 could certainly not have been anticipated, and reveal that localized enhancements in wind stress curl can significantly influence SST, in qualitative agreement with recent observations (e.g. Chelton *et al.*, 2001, 2004; O'Neill *et al.*, 2003, 2005).



6.1 Seasonal Dependencies

Figure 5 reveals a pronounced seasonal dependence in the sensitivity of J_{SST} to $\bar{\tau}$ and $\text{curl}\bar{\tau}$, with largest (smallest) sensitivities typically occurring during Fall (Spring). The sensitivity to $\bar{\tau}$ ($\text{curl}\bar{\tau}$) varies by a factor $\sim 2 - 6$ ($\sim 5 - 10$) over the course of a year. For $\gamma = 0$, the most sensitive period corresponds to the time when the upwelling favorable alongshore winds are generally weakening, a time when relatively small perturbations in an alongshore wind can yield significant changes in SST because near the surface $\partial T/\partial z$ is large nearshore (Fig. 3b). During Spring on the otherhand the alongshore winds are strongest and the thermocline outcrops offshore (Fig. 3a), exposing cold sub-thermocline waters with a smaller $\partial T/\partial z$, so that variations in alongshore wind are less effective at changing SST at this time. For the case $\gamma = 1$ (Fig. 5e) J_{SST} is sometimes sensitive to variations in $\bar{\tau}$ even when the alongshore winds are strong as evidenced by the wide envelope of the extremes during Spring depending on the size of the SST anomalies.

These results suggest that SST may be very susceptible to variations in the timing of the relaxation of alongshore winds at the end of the upwelling season. While Fig. 5 quantifies the time variability of this sensitivity in ROMS, such variations may also be manifested in the real ocean in relation to the broadest mesoscale circulation features of the CCS.

6.2 A Perturbation Interpretation

As noted in section 4, the gradient vectors are synonymous with perturbations that yield large changes in J because of their connection with the singular vectors of the TLROMS propagator. For the case $\gamma = 0$, J_{SST} is governed by the change in SST over the course of a month, and



$\partial J/\partial\bar{\tau}$ corresponds to perturbations in $\bar{\tau}$ that yield a large change in SST over the same period.

During Oct year 6, SST warms by $\sim 1^\circ\text{C}$ in the northern part of the target region, and cools in the south (Fig. 8a). Therefore a general increase in southerly alongshore wind enhances the northern warming trend, reduces the southern cooling trend, leading to an increase in J_{SST} , consistent with Figs. 7a and 7b if we view the sensitivity patterns as wind perturbations. The target region SST in Fig. 8a is associated with a pair of mesoscale features, identified as “ e_1 ” and “ e_2 ” in Fig. 2f that conspire to produce a filament of cold SST water offshore near 35°N , denoted “f” in Fig. 2e. Evolution of e_1 , e_2 and f can be influenced by suitably aligned wind stress perturbations that enhance or suppress developing waves. Figure 8b shows the pattern of $\partial J/\partial\tau$ for the period 21-25 Oct superimposed on SST for the same period, and reveals a pattern of cross-isotherm winds near 35°N (indicated by the grey box) within the band of cooling SST along the southern flank of filament f. Figure 8b shows a second similar feature near the Monterey Bay, indicated by a second grey box. These features can modify the development of SST anomalies, an idea confirmed by additional experiments in which NLRMS was forced by wind stress perturbations with the structure of $\partial J/\partial\tau$ in Fig. 8b. SST anomalies developed along the southern flank of filament f consistent with enhanced upwelling and downwelling and baroclinic wave development (not shown).

Similar arguments can be advanced to explain the spatial variations in the sensitivity of J_{SST} to wind stress curl apparent in Figs 7b and 7d. The change in sign of $\partial J/\partial\text{curl}\bar{\tau}$ on 21-25 Oct close to the coast (Fig. 7d), and the north-south dipole in $\partial J/\partial\text{curl}\bar{\tau}$ that develops along 123°W centered at 36°N suggests that subtle local changes in wind stress curl can modify the subsequent development of the e_1 -f- e_2 circulation complex and enhance J_{SST} .

The sensitivities displayed in Fig. 8 and the response of NLRMS to wind perturbations of



this form are both consistent with Spall (2007) who showed how air-sea interactions can produce feedbacks that enhance the development of baroclinically unstable waves. The correspondence between the sensitivities of Fig. 8 and Spall (2007) is not complete, however, because there are no coupled air-sea interactions in NLRMS. However, the NLRMS ocean eddy response to changes in the wind can have the same ocean dynamics as the Spall mechanism, only there is no ocean-induced feedback to change the wind, except insofar that the adjoint model reveals how the wind must change in order to enhance the growth of an eddy and the consequent effect on SST. Certainly the details of the spatio-temporal nature of the sensitivities to surface forcing like those of Fig. 8 could not have been anticipated without the adjoint model.

The time variations and year-to-year variability of the sensitivities of J_{SST} in Fig. 5e are therefore associated with a combination of sensitivity to the alongshore winds which drive changes in upwelling, and sensitivity to local wind forcing that promotes wave variability.

6.3 Sensitivity to surface heat flux

Figures 5c and 5f indicate that J_{SST} is typically least sensitive to variations in \bar{Q} during Spring, and most sensitive in the Fall, although for $\gamma = 1$ there are significant year-to-year variations due to variability in the mesoscale circulation. Sensitivity of J_{SST} to \bar{Q} typically varies by a factor $\sim 3 - 9$ during the course of a year. The spatio-temporal patterns of $\partial J / \partial \bar{Q}$ (not shown) reveal that J_{SST} is sensitive to local variations in \bar{Q} , and to the influence of horizontal advection by the mesoscale circulation.



7 Eddy Kinetic Energy (J_{KE}) and Baroclinic Instability ($J_{\sigma BI}$)

The sensitivity of J_{KE} in (7) to variations in $\bar{\tau}$ and $\text{curl}\bar{\tau}$ is summarized in Figs. 9a and 9b, where for brevity, we present only those results for the case where J_{KE} is an index of eddy kinetic energy (*i.e.* $\gamma = 1$). The sensitivity of J_{KE} to variations in \bar{Q} is 2 orders of magnitude weaker and not shown. Figure 9b reveals that J_{KE} is most sensitive to variations in $\bar{\tau}$, and indicates that there is no discernable seasonal variation in the average sensitivity to perturbations in wind stress. The envelope of extremes in sensitivity is typically widest in Spring and Fall when the sensitivity can vary by a factor $\sim 2 - 3$ during any given year. Figure 9a indicates a similar tendency for the sensitivity of J_{KE} to perturbations in wind stress curl.

Figures 10a and 10b illustrate typical patterns of $\partial J_{KE}/\partial\bar{\tau}$ and $\partial J_{KE}/\partial\text{curl}\bar{\tau}$; also shown are contours of SSH for the same periods as an indicator of the surface circulation. The patterns of sensitivity are complex but clearly related to the underlying circulation and exhibit considerable temporal variability (not shown) which could not be anticipated *a priori* in the absence of ADROMS. Regions of elevated sensitivity coincide mainly with the centers of eddies and meanders and with regions of confluent and diffluent flow. This is consistent with singular vector analyses by Farrell (1990) and Moore and Farrell (1993) in which such regions are favored for perturbation growth and secondary instability via barotropic processes, which Figs. 10a and 10b indicate can be induced by perturbations in the wind.

The sensitivity of the potential for baroclinic instability as measured by $J_{\sigma BI}$ in (8) is summarized in Figs. 9c and 9d. The sensitivity of $J_{\sigma BI}$ to variations in \bar{Q} is an order of magnitude smaller and not shown. When computing the sensitivities according to (5), the spatial and temporal variations of N are governed by the basic state flow. However, in the



Taylor expansion of σ_{BI} , perturbations in N are neglected, and we consider only variations in \mathbf{v} when computing $\partial G/\partial\Phi$ in (4). In all cases there is a weak seasonal cycle with maximum (minimum) sensitivities in the Spring and early Summer (Fall to Winter transition), a time when the wind-driven alongshore circulation is strongest and therefore more prone to instability due to the enhanced vertical shear.

Figures 10c and 10d illustrate typical patterns of $\partial J_{\sigma_{BI}}/\partial\bar{\tau}$ and $\partial J_{\sigma_{BI}}/\partial\text{curl}\bar{\tau}$, superimposed on contours of SSH for the same period. Despite the relatively large target area, the regions of maximum sensitivity with respect to $\bar{\tau}$ and $\text{curl}\bar{\tau}$ are confined to regions where the CC is coherent, narrow, and hugs the coast. These will be regions where changes in wind stress and wind stress curl can exert maximum impact on the potential for baroclinic instability through changes in the vertical shear brought about by upwelling-induced changes in stratification. Figure 10d, however, shows that there are considerable alongshore variations in sensitivity to $\text{curl}\bar{\tau}$ which could not have been anticipated *a priori*.

8 Summary and Conclusions

An adjoint method has been used to explore variations in the sensitivity to surface forcing of coastal SST and upwelling, EKE, and the potential for baroclinic instability of the complex circulation patterns that develop in the CCS. This is one of the first documented applications of adjoint sensitivity analysis for the coastal ocean circulation using an ocean general circulation model. New results and insights applicable to the broadest scale, persistent mesoscale circulations resolvable by the model include:

- (1) A formal quantification of ocean model circulation sensitivities to surface forcing, sensi-



tivities that are previously undocumented.

- (2) Identification and quantification of temporal variations in circulation sensitivities to surface forcing, sensitivities that are associated with seasonal variations in the underlying circulation and with variations in the ocean mesoscale circulation.
- (3) Identification and appreciation of the often complex nature of spatial variations in the circulation sensitivities to the surface forcing that are intimately tied to the structure of the underlying ocean circulation via wind-induced wave development and the evolution of forcing-induced perturbations controlled by localized barotropic and baroclinic processes and instabilities.
- (4) A clear separation of the circulation sensitivity to wind stress versus wind stress curl, a topic that has been much discussed in the oceanographic literature (e.g. Enriquez and Friehe, 1995).

SST along the central California coast is about equally sensitive to variations in wind stress and surface heat flux, although sensitivity to wind stress curl is also significant. The upwelling circulation displays greatest sensitivity to surface forcing variations during late Summer and Fall when upwelling favorable winds are relaxing, and least sensitivity during the Winter and Spring, the latter being the peak of the upwelling season. Summer sensitivities are typically some 2-4 times larger than in the Spring but larger variations (a factor $\sim 5 - 10$) do occur during some years. These results indicate that SST in the upwelling region will be sensitive to variations in the timing of the relaxation of the alongshore winds at the end of the upwelling season. The considerable year-to-year variations in sensitivity are controlled by the details of



the mesoscale circulations that develop in the model. Forcing perturbations that are appropriately aligned with the underlying circulation can significantly alter the development of the mesoscale circulation itself, a finding that has implications for the predictability of the CCS.

Eddy kinetic energy off the central coast exhibits no obvious seasonal cycle in sensitivity to surface forcing variations, although there is considerable interannual variability. The sensitivity varies by at most a factor of 2 over the course of a year, and variations in the spatial patterns of sensitivity are most likely controlled by variations in the stability of the circulation, which would explain the absence of seasonal variations in sensitivity strength.

The potential for baroclinic instability also displays seasonal trends and variations in sensitivity, being greatest during Spring when the horizontal temperature gradient near the coast is largest, which implies larger vertical shear and a greater tendency for the alongshore geostrophic flow to be baroclinically unstable. The greatest sensitivity is associated with variations in wind stress, and the sensitivity varies by about a factor of ~ 2 throughout the year although variations in wind stress curl are effective also. While our results largely confirm the importance of local wind forcing as reported by others, a new and unique aspect of this study is that the spatio-temporal sensitivities of the model CCS circulation to variations in surface forcing have been quantified. In all cases, the spatial variations in sensitivity were found to be complex and flow-dependent, and could not have been anticipated *a priori* without the adjoint model.

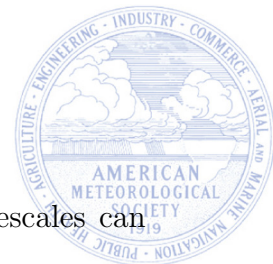
More generally, the 3-dimensional time evolving gradient vectors also aid in identifying the influence that specific physical processes, such as horizontal advection and instability, can exert on sensitivity. Recall that the sensitivities can be expressed as a linear superposition of the SVs of TLROMS. The structure of the gradient vectors is largely dictated by the fastest growing SVs of the target region circulation, and characteristic signatures of instabilities associated with



the dominant SVs are present in the gradient fields. For example, Fig. 11a shows $\partial J_{\text{SST}}/\partial\zeta$ for April year 6 for $\gamma = 1$, and reveals that isolines of $\partial J_{\text{SST}}/\partial\zeta$ tilt upstream against the current in the vicinity of the straining flow associated with the equatorward CC as it passes through the target area close to the coast. $\partial J_{\text{SST}}/\partial\zeta$ is synonymous with the sensitivity to variations in geostrophic stream function, and is an indicator of kinetic energy release from the CC by barotropic processes (Pedlosky, 1987, Chapter 7). The role of localized barotropic instability in controlling the evolution of the CC has received relatively little attention. Temporal variations and trends in $\partial J/\partial\zeta$ may be a potentially very useful indicator of variations in the sensitivity of J to growth by barotropic processes.

Similarly, sensitivity to baroclinic instability can be identified in as isoline tilts in the vertical as illustrated in Fig. 11b which shows a vertical section of $\partial J_{\text{SST}}/\partial v$ through the core of the CC. Tilts in isolines of $\partial J_{\text{SST}}/\partial v$ against the prevailing equatorward flow of the CC in the upper 200 m coincide with regions of large shear (Fig. 11c), features also present in other components of $\partial J_{\text{SST}}/\partial\Phi$ (not shown). Using such information to understand and quantify the sensitivities controlled by instability processes clearly deserves more attention.

One aspect of the circulation sensitivity not reported here but relevant to ocean prediction is the sensitivity to variations in the model initial conditions. While each index is an order of magnitude more sensitive to variations in the initial conditions than to variations in surface forcing, the forcing provides a weaker yet significant control on the processes considered, and contributes to temporal changes in the circulation as the forcing varies, thereby confusing the source of control. The pronounced seasonal variations in sensitivity suggest that correcting for uncertainties in the surface forcing may be most critical at the end of the upwelling season, and indicate that errors and uncertainties in surface forcing may significantly influence the



predictability of the circulation on monthly timescales. Such errors on these timescales can arise from errors in atmospheric forecast models as well from the inherent limit of predictability of the atmospheric circulation, which at middle latitudes is just a few days. The latter is associated with the chaotic nature of the atmospheric circulation, which on the timescales of the ocean circulation, can be viewed as a stochastic processes. Therefore, it would appear that the influence of stochastic forcing on the CCS may also be significant, particularly in relation to eddy generation through baroclinic processes. This will be the subject of a future study.

This work demonstrates that even the most basic, fundamental, and best understood features of the CCS circulation exhibit significant temporal and complex spatial variations in sensitivity to surface forcing that hitherto are undocumented and not previously recognized. The model sensitivities were found to be robust to changes in the wind forcing products used to drive the reference circulation $\Phi_0(t)$, and to changes in the configuration of the open boundary conditions. Additional experiments by Veneziani *et al.* (2008) using a similar model configuration and 10 km resolution yield qualitatively similar results to those reported here. The robust nature of the model results suggests that they may also be applicable to the sensitivity of the broadest observed energetic mesoscale features of the CCS to variations in surface forcing.

Acknowledgements

The work described here was supported by the Office of Naval Research (grant numbers N00014-06-1-0406, N00014-05-M-0277 and N00014-01-1-0209). Thanks also for the helpful comments of two anonymous reviewers.

Appendix

Since J in (6) involves a time integral, the expressions for the sensitivities given by (5) are modified. To demonstrate, we will re-express (6) in discretized form as:

$$J_{\text{SST}} = \frac{1}{N} \sum_{j=0}^N (\Phi(t_i + j\Delta t) - \gamma \bar{\Phi})^T \mathbf{H}(\Phi(t_i + j\Delta t) - \gamma \bar{\Phi}) \quad (\text{A1})$$

where \mathbf{H} is a diagonal matrix with non-zero elements (grid cell areas divided by the target area) only at those points that correspond to the SST gridpoints within the target polygon, and $\bar{\Phi}$ is the appropriate monthly mean value of Φ . The sensitivity of J_{SST} to variations in the initial conditions $\Phi_i = \Phi(t_i)$ is then given by (using (4)):

$$\frac{\partial J_{\text{SST}}}{\partial \Phi_i} = \frac{2}{N} \sum_{j=0}^N \mathbf{R}^T(t_i + j\Delta t, t_i) \mathbf{H}(\Phi(t_i + j\Delta t) - \gamma \bar{\Phi}) \quad (\text{A2})$$

which represents the solution of ADROMS when forced by $2\mathbf{H}(\Phi(t) - \gamma \bar{\Phi})/(N\Delta t)$.

Similarly, using (4) the sensitivity of J_{SST} to variations in the forcing is given by:

$$\frac{\partial J_{\text{SST}}}{\partial \mathbf{f}(t_i + k\Delta t)} = \frac{2\Delta t}{N} \sum_{m=k}^N \mathbf{P}^T \mathbf{R}^T(t_i + m\Delta t, t_i + k\Delta t) \mathbf{H}(\Phi(t_i + m\Delta t) - \gamma \bar{\Phi}). \quad (\text{A3})$$

Equation (A3) represents the solution of ADROMS forced by $2\mathbf{H}(\Phi(t) - \gamma \bar{\Phi})/N$. The sensitivity to variations in the time averaged forcing $\bar{\mathbf{f}}$, such as the time interpolated monthly means used here to drive the model, is given by:

$$\frac{\partial J_{\text{SST}}}{\partial \bar{\mathbf{f}}} = \frac{2\Delta t}{N} \sum_{j=0}^N \sum_{i=0}^j \mathbf{P}^T \mathbf{R}^T(t_i + j\Delta t, t_i + i\Delta t) \mathbf{H}(\Phi(t_i + j\Delta t) - \gamma \bar{\Phi}) \quad (\text{A4})$$

which represents the time integral of the forced ADROMS solution. It can be shown that (A4) also represents the sensitivity to variations in the interpolants when $\mathbf{f}(t)$ is computed by



interpolation between different realizations of $\bar{\mathbf{f}}$.

Even though there is no explicit variable for wind stress curl in ROMS, the sensitivity of J to variations in wind stress can be readily computed. If we denote wind stress curl as $c = \mathbf{k} \cdot \nabla \times \bar{\boldsymbol{\tau}}$, then using the D-operator method (Stephenson, 1973) it can be shown that $\partial J_{\text{SST}} / \partial c$ is given by the scalar function χ that is the solution of $\nabla^2 \chi = \mathbf{k} \cdot \nabla \times (\mathbf{i} \partial J_{\text{SST}} / \partial \bar{\tau}_x + \mathbf{j} \partial J_{\text{SST}} / \partial \bar{\tau}_y)$. The ROMS solution does not depend on wind stress or wind stress curl over land, so in these regions and along coastal boundaries it was assumed that $\chi = 0$. The boundary conditions on χ along open boundaries is undetermined, so we assume that $\chi = 0$ also. Methods for solving a Poisson equation on irregular ROMS grids in the presence of open boundaries using methods of control theory are discussed by Li *et al.* (2006) and will be explored in the future for the problem of computing χ .

PRELIMINARY ACCEPTED VERSION



References

- Abbot, M.R. and P.M. Zion, 1985: Satellite observations of phytoplankton variability during an upwelling event. *Cont. Shelf Res.*, **4**, 661-680.
- Aiken, C.M., A.M. Moore, and J.H. Middleton, 2002: The non-normal nature of recirculating flows in the coastal zone. *J. Phys. Oceanogr.*, **32**, 2955-2974.
- Allen, J.S., 1980: Models of wind-driven currents on the continental shelf. *Ann. Rev. Fluid Mech.*, **12**, 389-433.
- Auad, G., A. Parés-Sierra, and G.K. Vallis, 1991: *J. Phys. Oceanogr.*, **21**, 1534-1552.
- Bakun, A., 1990: Global climate change and intensification of coastal upwelling. *Science*, **247**, 198-201.
- Barth, J.A., 1994: Short-wavelength instabilities on coastal jets and fronts. *J. Geophys. Res.*, **99**, 16,095-16,115.
- Batteen, M.L., 1997: Wind-forced modeling studies of currents, meanders, and eddies in the California Current System. *J. Geophys. Res.*, **102**, 985-1010.
- Brink, K.H., 1991: Coastal-trapped waves and wind-driven currents over the continental shelf. *Ann. Rev. Fluid Mech.*, **23**, 389-412.
- Cacuci, D.G., 1981a: Sensitivity theory for nonlinear systems: I. Nonlinear functional analysis approach. *J. Math. Phys.*, **22**, 2794-2802.
- Cacuci, D.G., 1981b: Sensitivity theory for nonlinear systems: II. Extension to additional classes of response. *J. Math. Phys.*, **22**, 2803-2812.
- Capet, X., J.C. McWilliams, M.J. Molemaker and A.F. Shchepetkin, 2008: Mesoscale to sub-mesoscale transition in the California Current System. Part I: Flow structure, eddy flux,



and observational tests. *J. Phys. Oceanogr.*, **38**, 29-43.

Chao, Y., Z. Li, J. Farrara et al., 2007: Development, implementation and evaluation of a real-time ocean forecasting system for the Monterey Bay, California. *Deep Sea. Res.*, Submitted.

Chapman, D.C., 1985: Numerical treatment of cross-shelf open boundaries in a barotropic coastal ocean model. *J. Phys. Oceanogr.*, **15**, 1060-1075.

Chelton, D.B., R.A. DeSzoeko and M.G. Schlax, 1998: Geographical variability of the first baroclinic Rossby radius of deformation. *J. Phys. Oceanogr.*, **28**, 433-460.

Chelton, D.B., S.K. Esbensen, M.G. Schlax, N. Thum, M.H. Freilich, F.J. Wentz, C.L. Gentemann, M.J. McPhaden and P.S. Schopf, 2001: Observations of coupling between surface wind stress and sea surface temperature in the eastern tropical Pacific. *J. Climate*, **14**, 1479-1498.

Chelton, D.B., M.G. Schlax, M.H. Freilich and R.F. Milliff, 2004: Satellite measurements reveal persistent small-scale features in ocean winds. *Science*, **303**, 978-983.

Chelton, D.B., M.G. Schlax, R.M. Samelson and R.A. de Szoeko, 2006: Global observations of westward energy propagation in the ocean: Rossby waves or nonlinear eddies? Manuscript in preparation.

Chhak, K.C., A.M. Moore, R.F. Milliff, G. Branstator, W.R. Holland and M. Fisher, 2006: Stochastic forcing of the North Atlantic wind-driven ocean circulation. Part I: A Diagnostic Analysis of the Ocean Response to Stochastic Forcing. *J. Phys. Oceanogr.*, **36**, 300-315.

Chhak, K.C., A.M. Moore, R.F. Milliff, G. Branstator, W.R. Holland and M. Fisher, 2006: Stochastic forcing of the North Atlantic wind-driven ocean circulation. Part II: An Anal-



ysis of the Dynamical Ocean Response using Generalized Stability Theory. *J. Phys. Oceanogr.*, **36**, 316-334.

Chhak, K.C. and A.M. Moore, 2007: The North Atlantic Oscillation as a source of stochastic forcing of the wind-driven ocean circulation. *Dyn. Atmos. Oceans*, **43**, 151-170.

Chhak, K.C., A.M. Moore and R.F. Milliff, 2008: Stochastic forcing of ocean variability by the North Atlantic Oscillation. *J. Phys. Oceanogr.*, In press.

Di Lorenzo, E., 2003: Seasonal dynamics of surface circulation in the Southern California Current System. *Deep Sea Res. II*, **50**, 2371-2388.

Di Lorenzo, E., A.J. Miller, D.J. Neilson, B.D. Cornuelle and J.R. Moisan, 2004: Modeling observed California Current mesoscale eddies and the ecosystem response. *Int. J. Remote Sensing*, **25**, 1307-1312.

Di Lorenzo E., N. Schneider, K.M. Cobb, K.C. Chhak, P.J.S. Franks, A.J. Miller, J.C. McWilliams, S.J. Bograd, H.G. Arango, E. Curchister, T.M. Powell and P. Rivere, 2008: North Pacific gyre oscillation links ocean climate and ecosystem change. *Geophys. Res. Lett.*, **35**, L08607, doi:10.1029/2007GL032838.

Emery, W.J., W.G. Lee and L. Magaard, 1984: Geographic and seasonal distributions of Brunt-Väisälä frequency and Rossby radii in the North Pacific and North Atlantic. *J. Phys. Oceanogr.*, **14**, 294-316.

Enriquez, A.G. and C.A. Friehe, 1995: Effect of wind stress and wind stress curl variability on coastal upwelling. *J. Phys. Oceanogr.*, **25**, 1651-1671.

Farrell, B.F., 1990: Small error dynamics and predictability of flows. *J. Atmos. Sci.*, **47**, 2409-2416.



- Flather, R.A., 1976: A tidal model of the northwest European continental shelf. *Memoires de la Societe Royale des Sciences de Liege* 6 (10), 141-164.
- Frankignoul, C. and P. Müller, 1979: Quasi-geostrophic response of an infinite β -plane ocean to stochastic forcing by the atmosphere. *J. Phys. Oceanogr.*, **9**, 104-127.
- Franks, P.J.S., 2002: NPZ models of plankton dynamics: Their construction, coupling to physics, and application. *Journal of Oceanography*, **58**, 379-387.
- Galanti, E. and E. Tziperman, 2003: A midlatitude ENSO teleconnection mechanism via baroclinically unstable long Rossby waves. *J. Phys. Oceanogr.*, **33**, 1877-1888.
- Gelaro, R., R. Buizza, T.N. Palmer and E. Klinker, 1998: Sensitivity analysis of forecast errors and the construction of optimal perturbations using singular vectors. *J. Atmos. Sci.*, **55**, 1012-1037.
- Gill, A.E., 1982: *Atmosphere-Ocean Dynamics*. Academic Press, 662pp.
- Haidvogel, D.B., H.G. Arango, K. Hedstrom, A. Beckmann, P. Malanotte-Rizzoli and A.F. Shchepetkin, 2000: Model evaluation experiments in the North Atlantic basin: Simulations in nonlinear terrain-following coordinates. *Dyn. Atmos. Oceans*, **32**, 239-281.
- Haidvogel, D. B., H. Arango, W. P. Budgell, B. D. Cornuelle, E. Curchitser, E. Di Lorenzo, K. Fennel, W. R. Geyer, A. J. Hermann, L. Lanerolle, J. Levin, J. C. McWilliams, A. J. Miller, A. M. Moore, T. M. Powell, A. F. Shchepetkin, C. R. Sherwood, R. P. Signell, John C. Warner, and J. Wilkin, 2008: Ocean forecasting in terrain-following coordinates: Formulation and skill assessment of the Regional Ocean Modeling System. *J. Comput. Phys.*, **227**, 3595-3624.
- Hall, M.C.G. and D.G. Cacuci, 1983: Physical interpretation of the adjoint functions for sensitivity analysis of atmospheric models. *J. Atmos. Sci.*, **40**, 2537-2546.



- Hickey, B.M., 1979: The California Current System: hypotheses and facts. *Progress in Oceanography*, **8**, 191-279.
- Hickey, B.M., 1998: Coastal oceanography of western North America from the tip of Baja, California to Vancouver Island. *The Sea*, **11**, 345-393, Eds. A.R. Robinson and K.H. Brink, John Wiley and Sons.
- Hoskins, B.J. and P.J. Valdes, 1990: On the existence of storm-tracks. *J. Atmos. Sci.*, **47**, 1854-1864.
- Junge, M.M. and T.W.N. Haine, 2001: Mechanisms of North Atlantic wintertime sea surface temperature anomalies. *J. Climate*, **14**, 4560-4572.
- Kalnay, E., M. Kanamitsu, R. Kistler, W. Collins, D. Deaven, K. Gandin, M. Iredell, S. Saha, G. White, J. Woollen, Y. Zhu, M. Chelliah, W. Ebisuzaki, W. Higgins, J. Janowiak, K. Mo. C. Ropelewski, J. Wang, A. Leetmaa, R. Reynolds, R. Jenne and D. Joseph, 1996: NCEP/NCAR 40-years reanalysis project. *Bull. Amer. Meteor. Soc.*, **77**, 437-431.
- Kelly, K.A., R.C. Beardsley, R. Limeburner, K.H. Brink, J.D Paduan and T.K. Chereskin, 1998: Variability of the near-surface eddy kinetic energy in California Current based on altimetric, drifter, and moored current data. *J. Geophys. Res.*, **103**, 13,067-13,083.
- Large, W.G., J.C. McWilliams, and S.C. Doney, 1994: A review and model with a nonlocal boundary layer parameterization, *Rev. of Geophys.*, **32**, 363-403.
- Langland, R.H., R.L. Elsberry and R. Errico, 1995: Evaluation of physical processes in an idealized extratropical cyclone using adjoint sensitivity. *Quart. J. Roy. Meteor. Soc.*, **121**, 1349-1386.
- Li, Z., Y. Chao and J.C. McWilliams, 2006: Computation of the streamfunction and velocity potential for limited and irregular domains. *Mon. Wea. Rev.*, **134**, 3384-3394.



- Li, Z., Y. Chao, J.C. McWilliams and K. Ide, 2007: A three-dimensional variational data assimilation scheme for the regional ocean modeling system. *J. Atmos. Ocean. Tech.*, Submitted.
- Lindzen, R.S. and B.F. Farrell, 1980: A simple approximate result for the maximum growth rate of baroclinic instabilities. *J. Atmos. Sci.*, **37**, 1648-1654.
- McCreary, J.P., P.K. Kundu and S.Y. Chao, 1987: On the dynamics of the California Current System. *J. Marine Res.*, **45**, 1-32.
- McCreary, J.P., Y. Fukamachi and P.K. Kundu, 1991: A numerical investigation of jets and eddies near an eastern ocean boundary. *J. Geophys. Res.*, **91**, 2515-2534.
- Marchesiello, P., J.C. McWilliams and A. Shchepetkin, 2001: Open boundary conditions for long-term integration of regional oceanic models. *Ocean Modelling*, **3**, 1-20.
- Marchesiello, P., J.C. McWilliams and A. Shchepetkin, 2003: Equilibrium structure and dynamics of the California Current System. *J. Phys. Oceanogr.*, **33**, 753-783.
- Miller, A.J., J.C. McWilliams, N. Schneider, J.S. Allen, J.A. Barth, R.C. Beardsley, F.P. Chavez, T.K. Chereskin, C.A. Edwards, R.L. Haney, K.A. Kelly, J.C. Kindle, L.N. Ly, J.R. Moisan, M.A. Noble, P.P. Niiler, L.Y. Oey, F.B. Schwing, R.K. Shearman and M.S. Swenson, 1999: Observing and modeling the California Current system. *EOS Transactions*, **80**, 533-539.
- Moore, A.M., H.G. Arango, E. Di Lorenzo, B.D. Cornuelle, A.J. Miller and D.J. Neilson, 2004: A comprehensive ocean prediction and analysis system based on the tangent linear and adjoint of a regional ocean model. *Ocean Modelling*, **7**, 227-258.
- Moore, A.M., H.G. Arango, E. Di Lorenzo, C.V.W. Lewis, T.M. Powell, B.D. Cornuelle and A.J. Miller, 2006: An adjoint sensitivity analysis of the southern California Current



circulation and ecosystem. Part II: The biological circulation. In preparation.

Moore, A.M. and B.F. Farrell, 1993: Rapid perturbation growth on spatially and temporally varying oceanic flows using an adjoint method: Application to the Gulf Stream. *J. Phys. Oceanogr.*, **23**, 1682-1702.

Müller, P. and C. Frankignoul, 1981: Direct atmospheric forcing of geostrophic eddies. *J. Phys. Oceanogr.*, **11**, 287-308.

O'Neill, L.W., D.B. Chelton and S.K. Esbensen, 2003: Observations of SST-induced perturbations of the wind stress field over the Southern Ocean on seasonal timescales. *J. Climate*, **16**, 2340-2354.

O'Neill, L.W., D.B. Chelton, S.K. Esbensen and F.J. Wentz 2005: High-resolution satellite measurements of the alongshore atmospheric boundary layer response to SST variations along the Agulhas return current. *J. Climate*, **18**, 2706-2723.

Oey, L.Y., 1999: A forcing mechanism for the poleward flow off the southern California coast. *J. Geophys. Res.*, **104**, 13,529-13,539.

Pedlosky, J., 1987: *Geophysical Fluid Dynamics*. 2nd Edition. Springer Verlag, pp710.

Perlin, N., R.M. Samelson and D.B. Chelton, 2004: Scatterometer and model wind and wind stress in the OregonNorthern California Coastal Zone. *Mon. Wea. Rev.*, **132**, 2110-2129.

Powell, T.M., C.V.W. Lewis, E.N. Curchister, D.B. Haidvogel, A.J. Hermann and E.L. Dobins, 2006: Results from a three-dimensional, nested biological-physical model of the California Current system and comparisons with statistics from satellite imagery. *J. Geophys. Res.*, In press.

Rabier, F., P. Courtier, J. Pailleuz and A. Hollingsworth, 1006: Sensitivity pf forecast errors to initial conditions. *Quart. J. Royal. Meteorol. Soc.*, **122**, 121-150.



- Shchepetkin, A.F. and J.C. McWilliams, 2004: The regional oceanic modeling system (ROMS): a split explicit, free-surface, topography-following-coordinate oceanic model. *Ocean Modelling*, **9**, 347-404.
- Spall, M.A., 2007: Effect of sea surface temperature-wind stress coupling on baroclinic instability in the ocean. *J. Phys. Oceanogr.*, **37**, 1092-1097.
- Stephenson, G., 1973: *Mathematical Methods for Science Students*. Longman, 528pp.
- Strub, P.T., P.M. Kosro, A. Huyer and CTZ collaborators, 1991: The nature of the cold filaments in the California Current System. *J. Geophys. Res.*, **96**, 14743-14768.
- Strub, P.T. and C. James, 2000: Altimeter-derived variability of surface velocities in the California Current System: 2. Seasonal circulation and eddy statistics. *Deep Sea Res.*, Part II, **47**, 831-870.
- Swenson, M.S., P.P. Niiler, K.H. Brink and M.R. Abbot, 1992: Drifter observations of a cold filament off Point Arena, California, in July 1988. *J. Geophys. Res.*, **97**, 3593-3610.
- Veneziani, M., C.A. Edwards and A.M. Moore, 2007: A Central California modeling study. Part II: Adjoint sensitivities to local and remote driving mechanisms. *J. Phys. Oceanogr.*, In preparation.
- Wilks, D.S., 1995: *Statistical Methods in the Atmospheric Sciences*. Academic Press, 467pp.



Figure Captions

Figure 1: (a) A map showing the location of the dominant topographic features that are known to influence the CCS. (b) The ROMS model domain and contours of bathymetry. The contour interval is 500 m.

Figure 2: The climatological mean SST for (a) April and (b) Oct computed from a 10 year integration of ROMS. Snap-shots of SST and SSH are shown for 1 April (c and d) and for 1 Oct (e and f) of year 6. The target areas used to define J_{SST} and J_{KE} are also identified. The filament labeled “f” in (e) and eddies labeled “e₁” and “e₂” in (f) are referred to in the main text.

Figure 3: Vertical cross-sections of the monthly mean temperature (degrees C) along the section indicated in Fig. 2e for the upper 300 m of the water column for (a) April and (b) Oct, computed from the 10 year integration. The 12°C isotherm is highlighted in white, and the contour interval is 1°C. Cross-sections along the same section of the monthly mean alongshore velocity (m s^{-1}) over the upper 1000 m are shown in (c) and (d) for April and Oct respectively. The zero contour separating poleward and equatorward flow is highlighted in white in (c) and (d), and the contour interval is 0.02 m s^{-1} .

Figure 4: Timeseries of (a) J_{SST} (K^2) and (b) J_{KE} ($\text{kg m}^{-1}\text{s}^{-2}$) for $\gamma = 0$ (dashed line) and 1 (solid line), and (c) $J_{\sigma_{\text{BI}}}$ (days^{-2}) computed from the last 8 years of the model integration for the target areas identified in Figs. 2a and 2b. The ordinate on the left (right) is for $\gamma = 0$ ($\gamma = 1$).

Figure 5: Timeseries of the monthly mean ΔJ_{SST} (solid line) associated with a one standard deviation change in (a,d) $\text{curl } \bar{\tau}$, (b,e) $\bar{\tau}$, and (c,f) \bar{Q} , applied at all points within the target

region identified in Fig. 2a and applied at all times, and computed from years 5-10. The panels on the left (right) is for $\gamma = 0$ ($\gamma = 1$). The dashed lines show the maximum and minimum values of ΔJ_{SST} encountered during each month for the same 5 year period. In the case of wind stress, the values of ΔJ_{SST} were computed for perturbations in both components of the vector.

Figure 6: Vectors of $(\partial J_{\text{SST}}/\partial \bar{\tau}_x, \partial J_{\text{SST}}/\partial \bar{\tau}_y)$ for Oct year 6 for (a) $\gamma = 0$ and (b) $\gamma = 1$. The target area that defines J_{SST} is shown in each case. The vector scaling is different in panels (a) and (b).

Figure 7: A close-up of (a,c) $(\partial J_{\text{SST}}/\partial \bar{\tau}_x, \partial J_{\text{SST}}/\partial \bar{\tau}_y)$ plotted as vectors, and (b,d) $\partial J_{\text{SST}}/\partial \text{curl } \bar{\tau}$ for the time intervals indicated during Oct year 6 for $\gamma = 0$. In (b) and (d) the contour interval is $6000 \text{ K N}^{-1} \text{ m}^3$, and the vectors in (a) and (c) are scaled the same.

Figure 8: (a) The difference in SST between Oct 30 and Oct 1 year 6. (b) Vectors of $(\partial J_{\text{SST}}/\partial \bar{\tau}_x, \partial J_{\text{SST}}/\partial \bar{\tau}_y)$ for the period 21-25 Oct year 6 superimposed on contours of SST for the same period. The grey boxes indicate regions where the sensitivity vectors cross SST contours, and where winds perturbations with these structures can modify the circulation by exciting growing or decaying baroclinic waves. The target region for JSST is shown in each case.

Figure 9: Timeseries of monthly mean ΔJ_{KE} (solid line) associated with a one standard deviation change in (a) $\text{curl } \bar{\tau}$, and (b) $\bar{\tau}$, applied at all points within the target region identified in Fig. 2b and applied at all times for $\gamma = 1$, and computed from years 5-10. The dashed lines show the maximum and minimum values of ΔJ_{KE} encountered during each month for the same 5 year period. Similar timeseries are shown of monthly mean $\Delta J_{\sigma_{\text{BI}}}$ associated with a

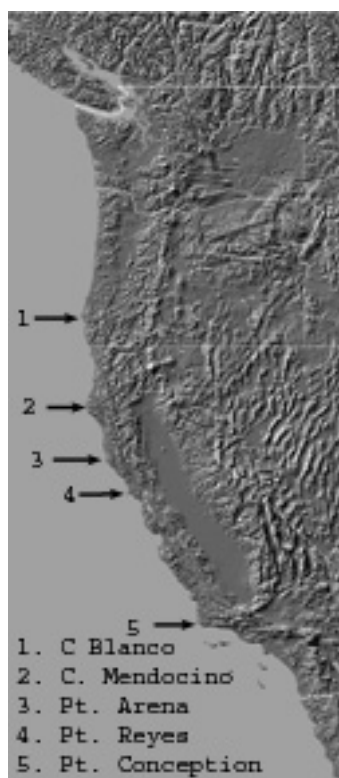
one standard deviation change in (c) $\text{curl } \bar{\tau}$, and (d) $\bar{\tau}$.

Figure 10: April year 6: (a) Vectors of $(\partial J_{\text{KE}}/\partial \bar{\tau}_x, \partial J_{\text{KE}}/\partial \bar{\tau}_y)$, (b) shaded contours of $\partial J_{\text{KE}}/\partial \text{curl} \bar{\tau}$, (c) vectors of $(\partial J_{\sigma_{\text{BI}}}/\partial \bar{\tau}_x, \partial J_{\sigma_{\text{BI}}}/\partial \bar{\tau}_y)$, and (d) shaded contours of $\partial J_{\sigma_{\text{BI}}}/\partial \text{curl} \bar{\tau}$. Also shown in each panel are contours of SSH which are the black contours in panels (a) and (c) and the white contours in (b) and (d). The contour interval for SSH is 0.05 m. The target regions for J_{KE} and $J_{\sigma_{\text{BI}}}$ are shown in each panel.

Figure 11: (a) Contour maps of $\partial J_{\text{SST}}/\partial \zeta$ for April year 6 for $\gamma = 1$. Contours of SSH for the same period are shown in white. (b) A vertical section of $\partial J_{\text{SST}}/\partial v$ over the upper 500 m along the section denoted AB in (a). Tilts of the isolines in the vertical against the alongshore flow are indicated by the black lines. (c) A vertical section of the monthly mean alongshore velocity over the upper 500 m along the section denoted AB in (a).

PRELIMINARY ACCEPTED VERSION

a



b

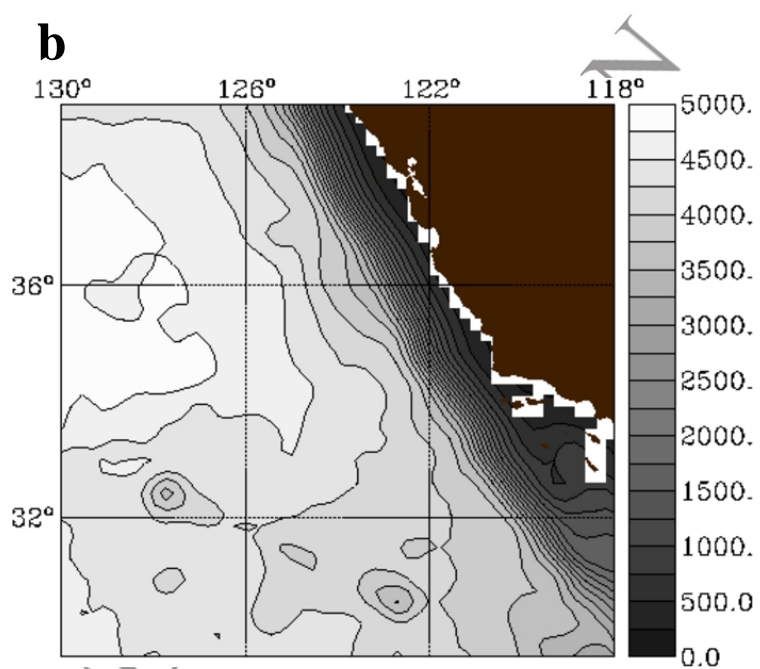


Figure 1: (a) A map showing the location of the dominant topographic features that are known to influence the CCS. (b) The ROMS model domain and contours of bathymetry. The contour interval is 500m.

PRELIMINARY ACCI

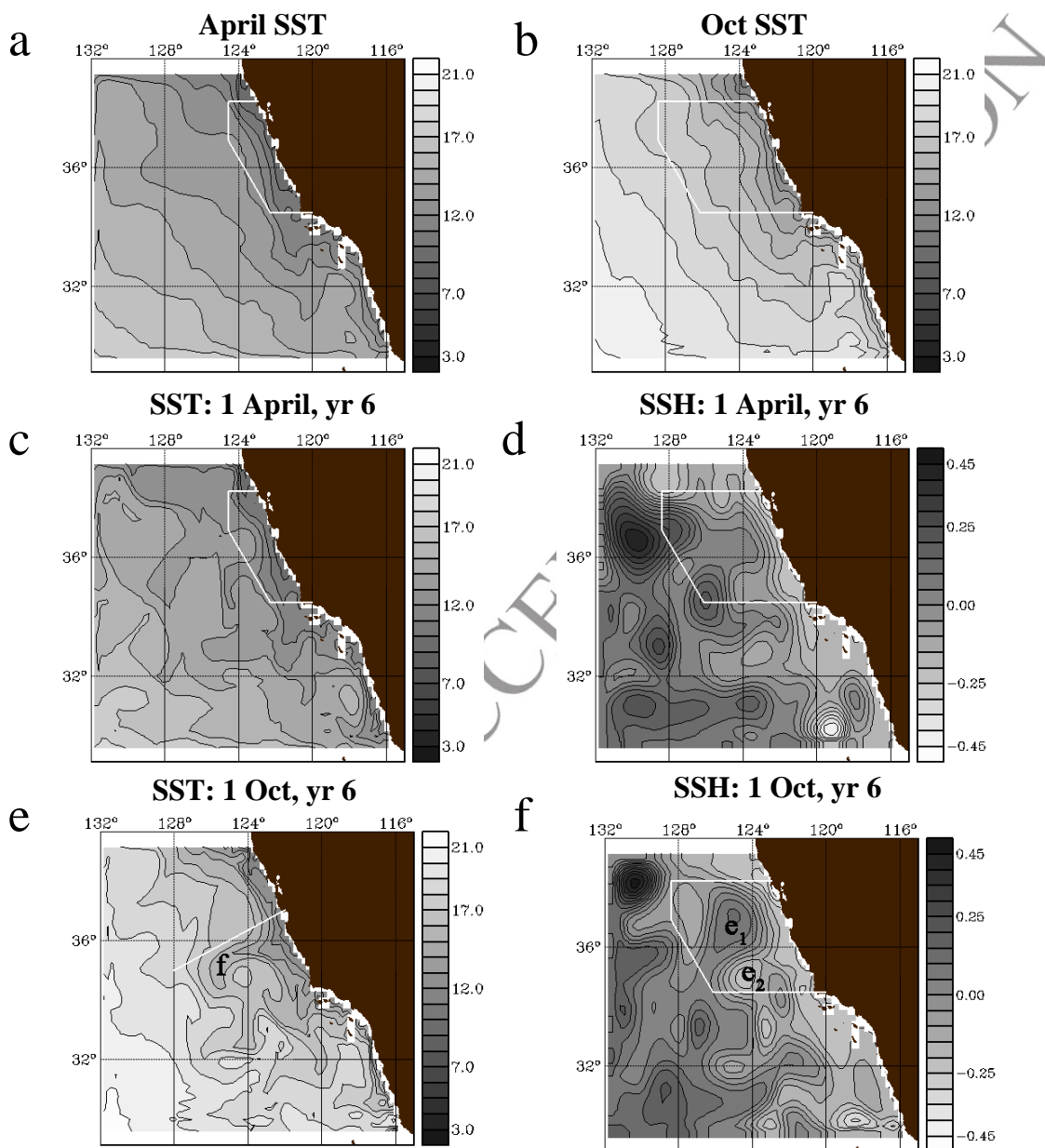


Figure 2: The climatological mean SST for (a) April and (b) Oct computed from a 10 year integration of ROMS. Snap-shots of SST and SSH are shown for 1 April (c and d) and for 1 Oct (e and f) of year 6. The target areas used to define J_{SST} and J_{KE} are also identified. The filament labeled “f” in (e) and eddies labeled “e₁” and “e₂” in (f) are referred to in the main text.

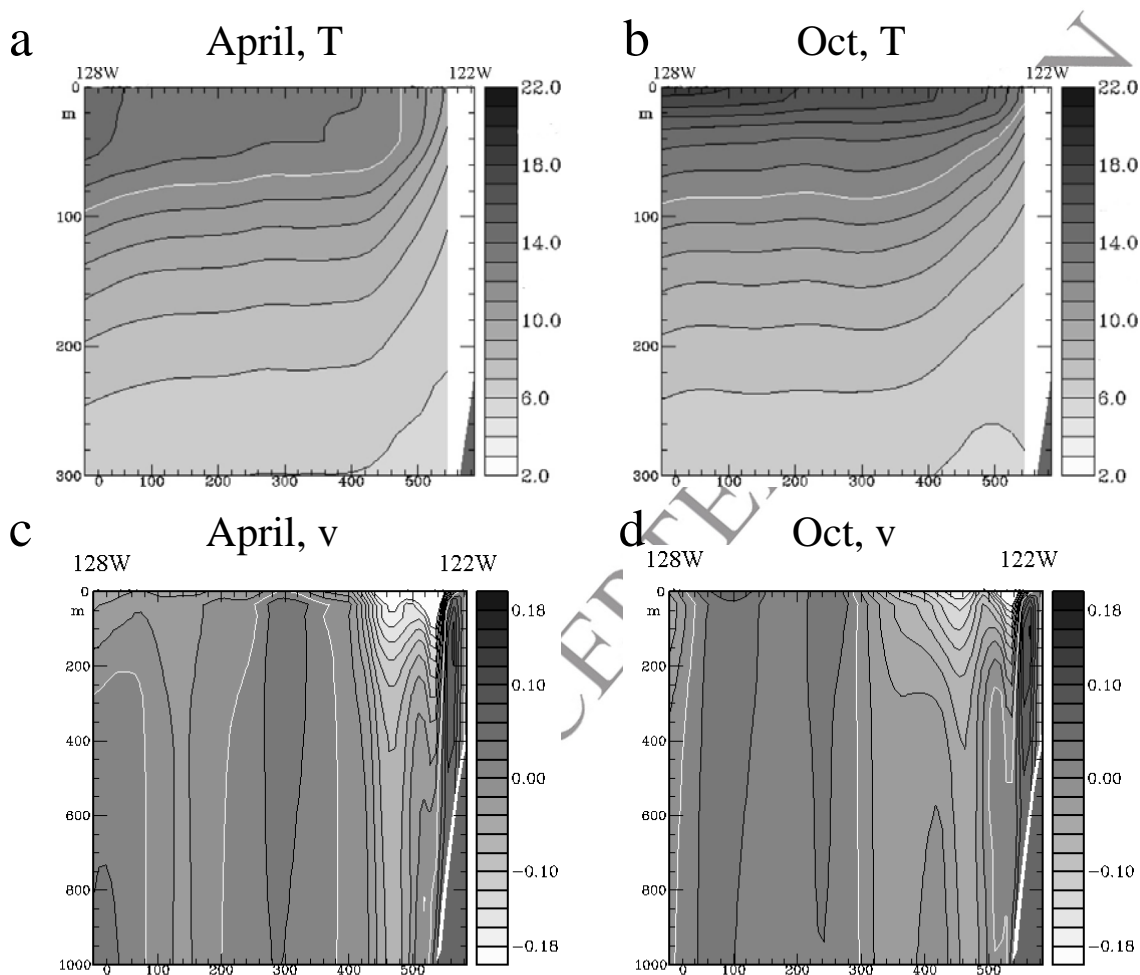


Figure 3: Vertical cross-sections of the monthly mean temperature (degrees C) along the section indicated in Fig. 2e for the upper 300m of the water column for (a) April and (b) Oct, computed from the 10 year integration. The 12C isotherm is highlighted in white, and the contour interval is 1C. Cross-sections along the same section of the monthly mean alongshore velocity (ms^{-1}) over the upper 1000m are shown in (c) and (d) for April and Oct respectively. The zero contour separating poleward and equatorward flow is highlighted in white in (c) and (d), and the contour interval is 0.02 m s^{-1} .

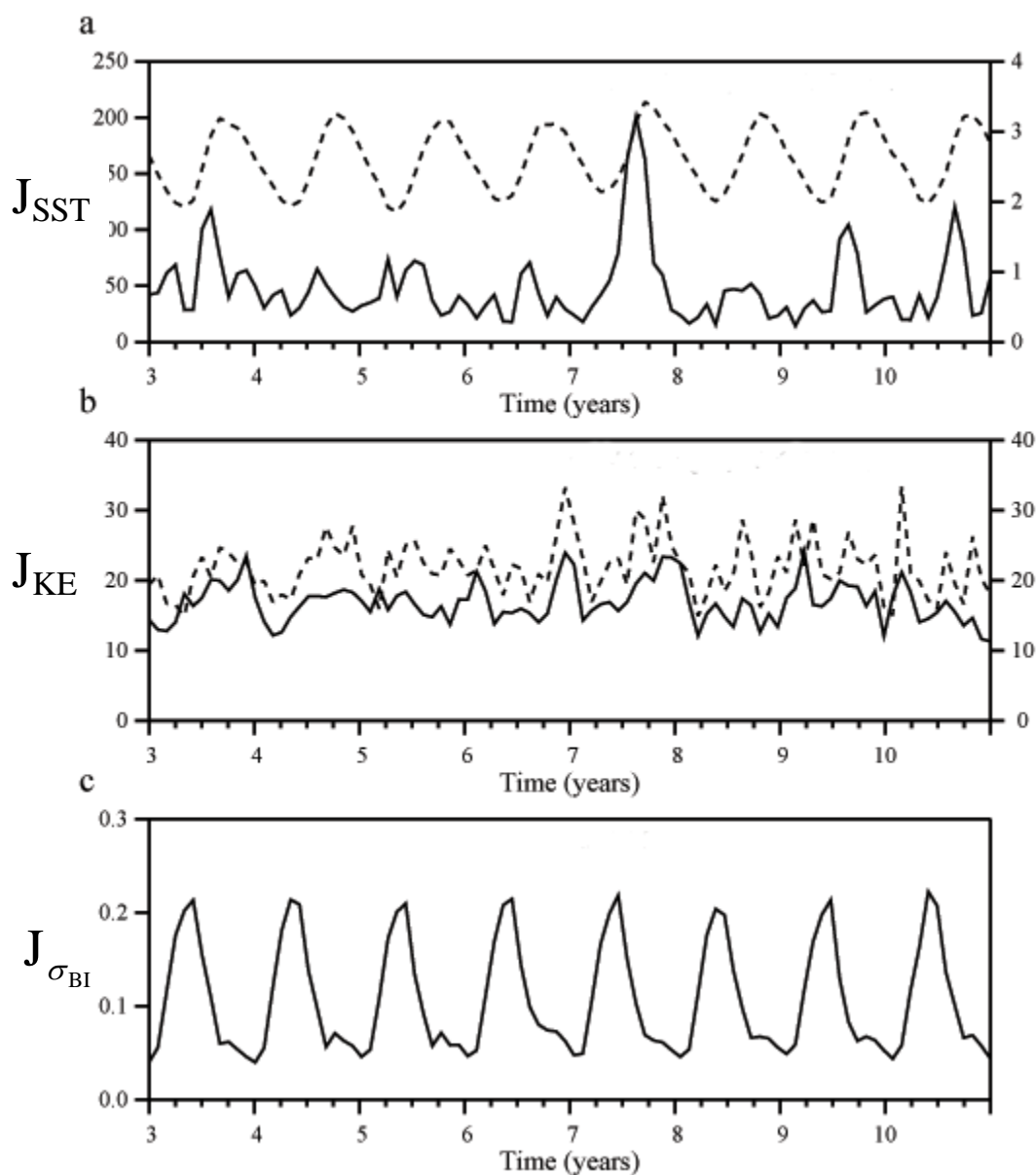


Figure 4: Time series of (a) J_{SST} (K²) and (b) J_{KE} (kg m⁻¹s⁻²) for $\gamma=0$ (dashed line) and $\gamma=1$ (solid line), and (c) $J_{\sigma_{BI}}$ (days⁻²) computed from the last 8 years of the model integration for the target areas identified in Figs. 2a and 2b. The ordinate on the left (right) is for $\gamma=0$ ($\gamma=1$).

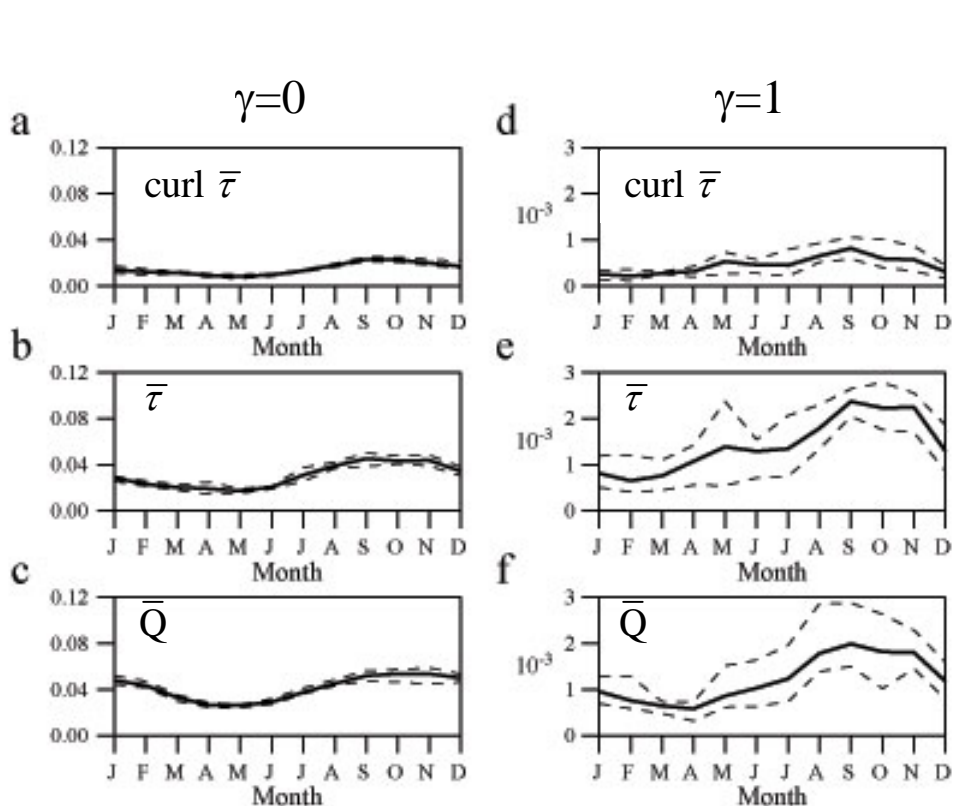


Figure 5: Timeseries of the monthly mean ΔJ_{SST} (K^2) (solid curve) associated with a one standard deviation change in (a,d) $\text{curl } \bar{\tau}$, (b,e) $\bar{\tau}$, and (c,f) \bar{Q} , applied at all points within the target region identified in Fig. 2a and applied at all times, and computed from years 5-10. The panels on the left (right) are for the case $\gamma=0$ ($\gamma=1$). The dashed lines show the maximum and minimum values of ΔJ_{SST} encountered during each month for the same 5 year period. In the case of wind stress the values of ΔJ_{SST} were computed for perturbations in both components of the vector.

PRELIMINARY

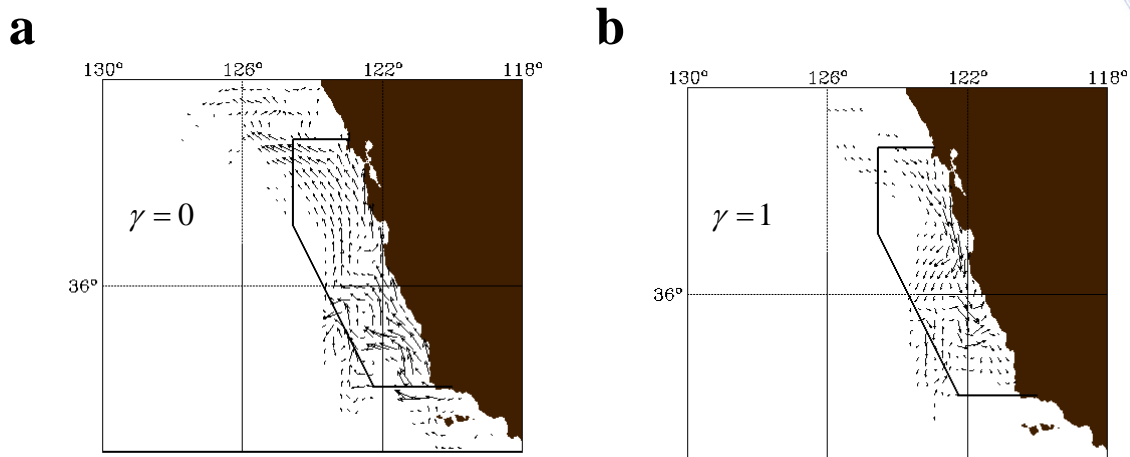


Figure 6: Vectors of $(\partial J_{\text{SST}}/\partial \bar{\tau}_x, \partial J_{\text{SST}}/\partial \bar{\tau}_y)$ for Oct year 6 for (a) $\gamma=0$, and (b) $\gamma=1$. The target area that defines J_{SST} is shown in each case. The vector scaling is different in panels (a) and (b).

PRELIMINARY ACCEPTED

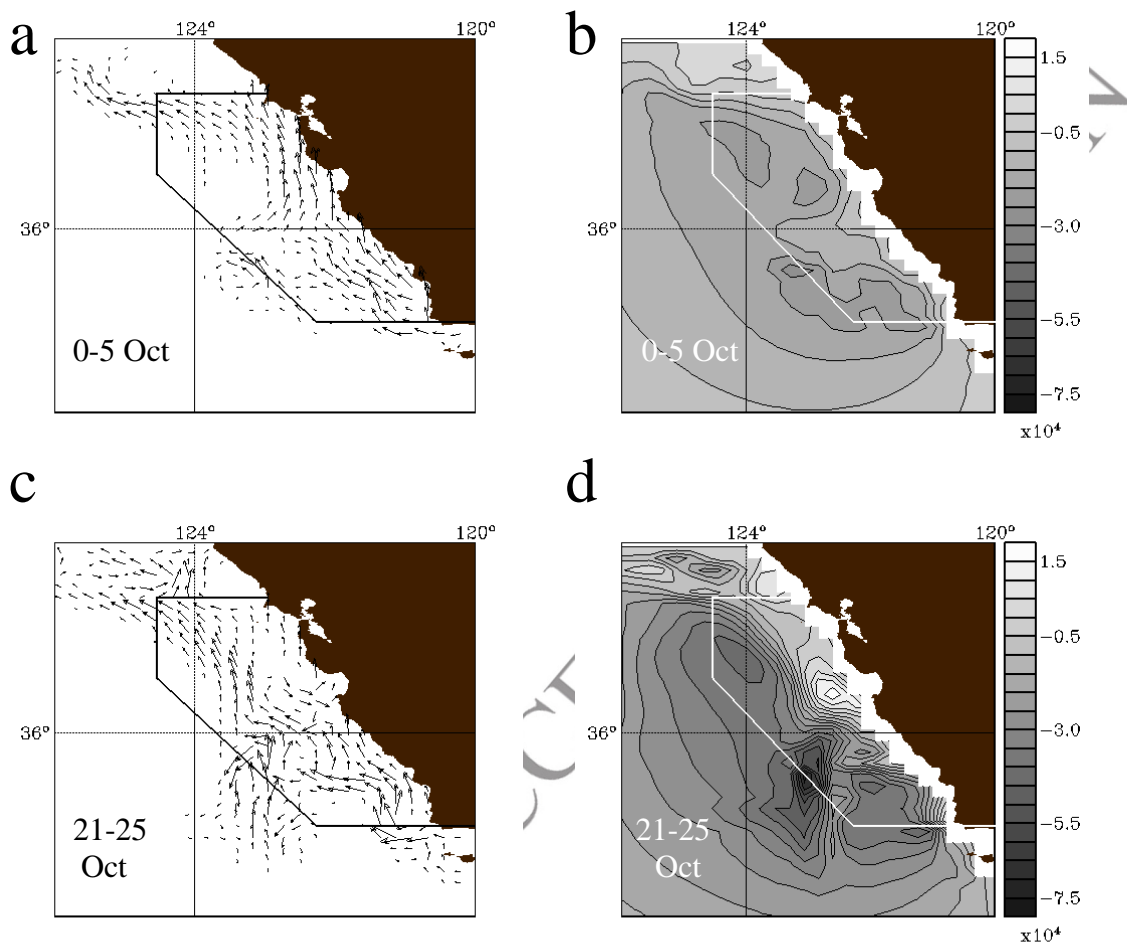


Figure 7: A close-up of (a,c) $(\partial J_{\text{SST}}/\partial \bar{\tau}_x, \partial J_{\text{SST}}/\partial \bar{\tau}_y)$ plotted as vectors, and (b,d) $\partial J_{\text{SST}}/\partial \text{curl} \bar{\tau}$ for the time intervals indicated during Oct year 6 for $\gamma=0$. In (b) and (d) the contour interval is $6000 \text{ KN}^{-1} \text{ m}^3$, and the vectors in (a) and (c) are scaled the same.

PRELIMINARY

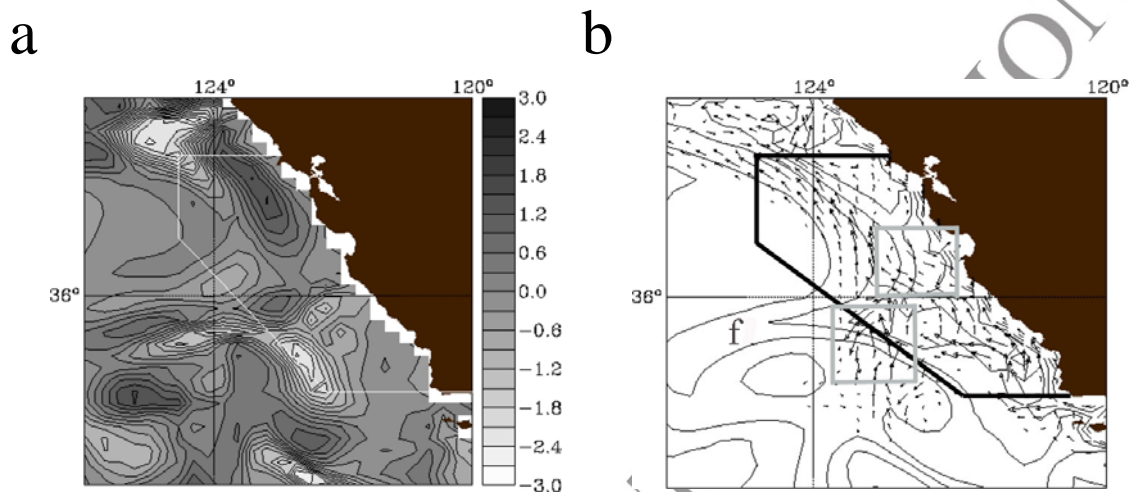


Figure 8: (a) The difference in SST between Oct 30 and Oct 1 year 6. (b) Vectors of $(\partial J_{SST}/\partial \bar{\tau}_x, \partial J_{SST}/\partial \bar{\tau}_y)$ for the period 21-25 Oct, year 6 superimposed on contours of SST for the same period. The grey boxes indicate regions where the sensitivity vectors cross the SST contours, and where winds perturbations with these structures can modify the circulation by exciting growing or decaying baroclinic waves. The target region for J_{SST} is shown in each case.

PRELIMINARY ACCEPTED

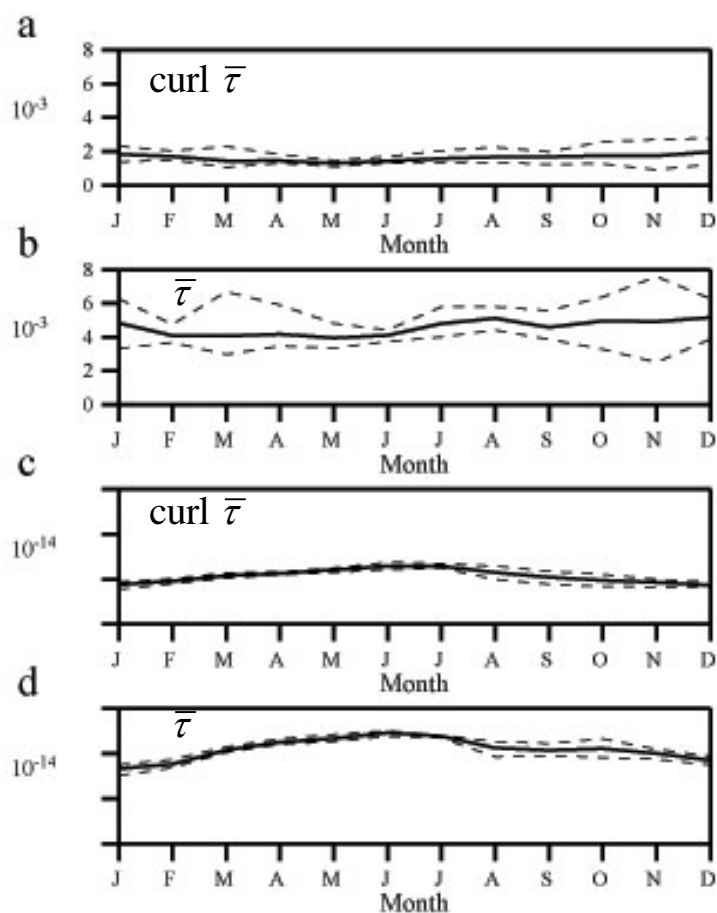


Figure 9: Timeseries of the monthly mean ΔJ_{KE} (solid line) associated with a one standard deviation change in (a) $\text{curl } \bar{\tau}$, and (b) $\bar{\tau}$ applied at all points within the target region identified in Fig. 2b and applied at all times for $\gamma=1$, and computed from years 5-10. The dashed lines show the maximum and minimum values of ΔJ_{KE} encountered during each month for the same 5 year period. Similar time series are shown of monthly mean $\Delta J_{\sigma_{BI}}$ associated with a one standard deviation change in (c) $\text{curl } \bar{\tau}$, and (d) $\bar{\tau}$.

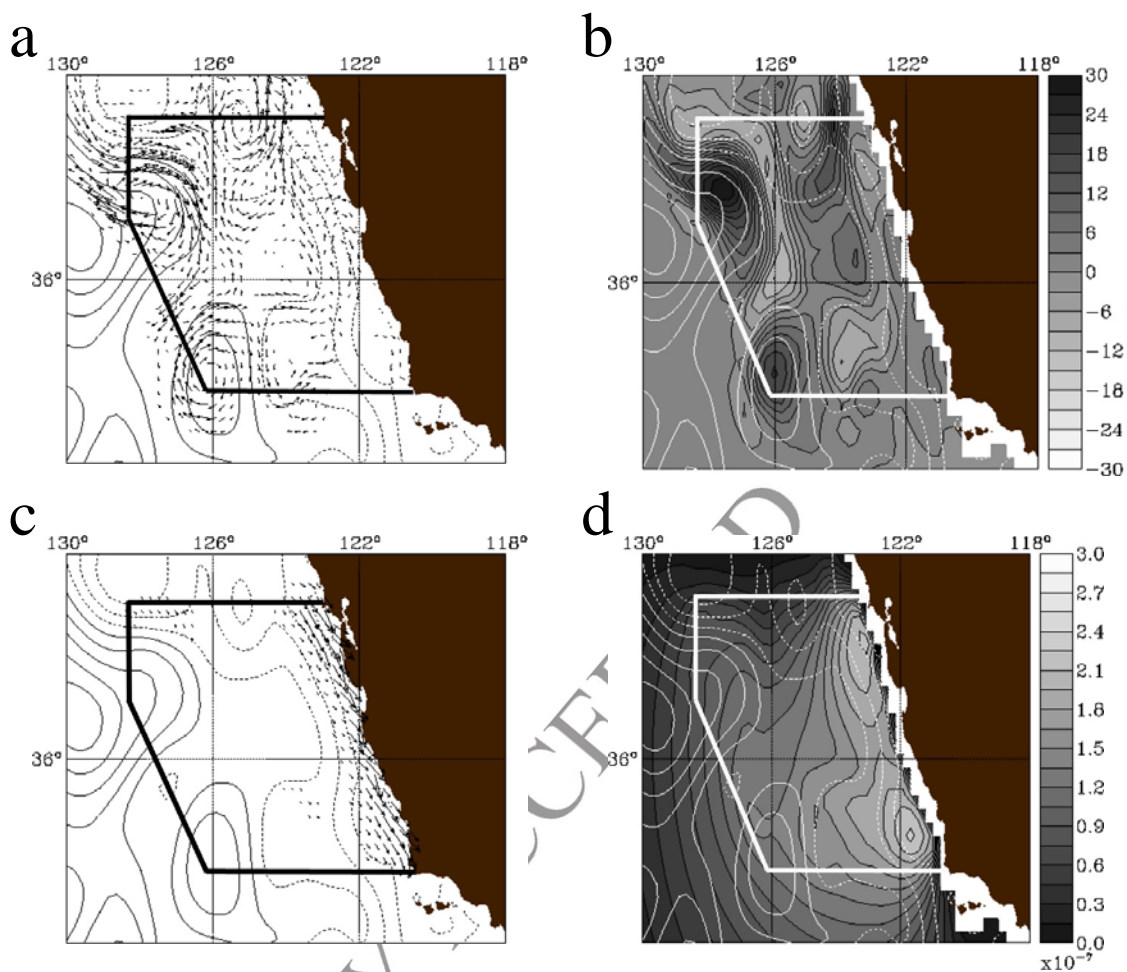


Figure 10: April year 6: (a) Vectors of $(\partial J_{KE}/\partial \bar{\tau}_x, \partial J_{KE}/\partial \bar{\tau}_y)$ and (b) shaded contours of $\partial J_{KE}/\partial \text{curl} \bar{\tau}$, (c) vectors of $(\partial J_{\sigma_{BI}}/\partial \bar{\tau}_x, \partial J_{\sigma_{BI}}/\partial \bar{\tau}_y)$, and (d) shaded contours of $\partial J_{\sigma_{BI}}/\partial \text{curl} \bar{\tau}$. Also shown in each panel are contours of SSH for April which are the black contours in panels (a) and (c) and the white contours in (b) and (d). The contour interval for SSH is 0.05m. The target regions for J_{KE} and $J_{\sigma_{BI}}$ are shown in each panel.

PRELIMINARY

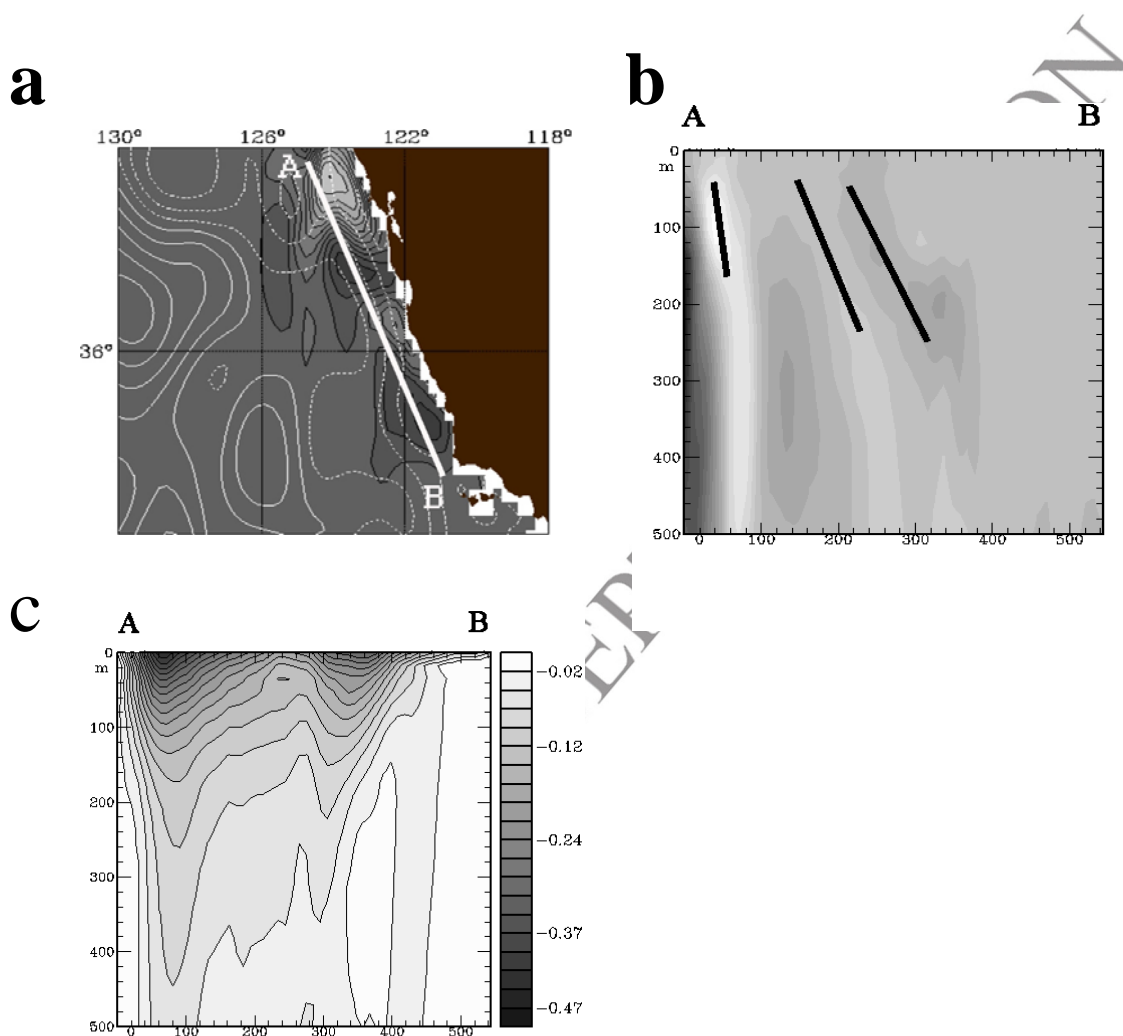


Figure 11: (a) Contour map of $\partial J_{SST}/\partial \zeta$ for April year 6 for $\gamma=1$. Contours of SSH for the same period are shown in white. (b) A vertical section of $\partial J_{SST}/\partial v$ over the upper 500 m along the section denoted AB in (a). Tilts of the isolines in the vertical against the alongshore flow are indicated by the black lines. (c) A vertical section of the monthly mean alongshore velocity over the upper 500 m along the section denoted AB in (a).